Eur. Phys. J. C 36, 341–363 (2004)
Digital Object Identifier (DOI) 10.1140/epjc/s2004-01948-4

THE EUROPEAN PHYSICAL JOURNAL C

Four-fermion production at $\gamma\gamma$ colliders: 1. Lowest-order predictions and anomalous couplings

A. Bredenstein, S. Dittmaier, M. Roth

Max-Planck-Institut für Physik (Werner-Heisenberg-Institut), 80805 München, Germany

Received: 19 May 2004 /
Published online: 16 July 2004 –

Abstract. We have constructed a Monte Carlo generator[1] for lowest-order predictions for the processes $\gamma\gamma \to 4f$ and $\gamma\gamma \to 4f\gamma$ in the standard model and extensions thereof by an effective $\gamma\gamma H$ coupling as well as anomalous triple and quartic gauge-boson couplings. Polarization is fully supported, and a realistic photon beam spectrum can be taken into account. For the processes $\gamma\gamma \to 4f$ all helicity amplitudes are explicitly given in a compact form. The presented numerical results contain, in particular, a survey of cross sections for representative final states and their comparison to results obtained with the program package Whizard/Madgraph. The impact of a realistic beam spectrum on cross sections and distributions is illustrated. Moreover, the size of various contributions to cross sections, such as from weak charged- or neutral-current, or from strong interactions, is analyzed. Particular attention is paid to W-pair production channels $\gamma\gamma \to WW \to 4f(\gamma)$ where we investigate the impact of background diagrams, possible definitions of the W-pair signal, and the issue of gauge-invariance violation caused by finite gauge-boson widths. Finally, the effects of triple and quartic anomalous gauge-boson couplings on cross sections as well as the possibility to constrain these anomalous couplings at future $\gamma\gamma$ colliders are discussed.

1 Introduction

A photon (or $\gamma\gamma$) collider [1] as an option at a future e^+e^- linear collider extends the physics potential of such a machine substantially. It provides us with information about new physics phenomena, such as properties of the Higgs boson or of new particles, which is in many respects complementary in the e^+e^- and $\gamma\gamma$ modes (see, e.g., [1,2] and references therein). For instance, Higgs-boson production in the s-channel [1–4] becomes accessible which is highly suppressed in e^+e^- annihilation, but very interesting for Higgs bosons of relatively large mass. Owing to its large cross section, W-pair production is of particular interest at a $\gamma\gamma$ collider. For instance, it can be used for precision tests of the gauge sector of the electroweak standard model (SM). While the reaction $e^+e^- \to WW$ depends on the gauge-boson couplings ZWW and γWW, the corresponding reaction at a $\gamma\gamma$ collider, $\gamma\gamma \to WW$, is sensitive to the gauge-boson couplings γWW and $\gamma\gamma WW$. At an e^+e^- collider the coupling $\gamma\gamma WW$ is only directly accessible through the bremsstrahlung process $e^+e^- \to WW\gamma$ which is suppressed by a factor $\alpha(0)/\pi$ with respect to the non-radiative process $e^+e^- \to WW$. Therefore, the sensitivity to the anomalous $\gamma\gamma WW$ coupling in the $\gamma\gamma$ mode is expected to be an order of magnitude better than in the e^+e^- mode. The precision for the measurement of the γWW coupling is comparable in both modes [5].

Since W bosons decay into fermion–anti-fermion pairs, the actually observed final states of $\gamma\gamma \to WW$ involve four fermions. Lowest-order predictions for $\gamma\gamma \to 4f$ processes (with monochromatic photon beams and leptonic or semi-leptonic final states) were discussed in [6,7]. With the exception of [8], the existing analyses on non-standard couplings at a $\gamma\gamma$ collider, which focus on anomalous triple gauge-boson couplings (ATGC) [5,9], on anomalous quartic gauge-boson couplings (AQGC) [3,10], on CP-violating gauge-boson couplings [11], and on effects of strongly interacting longitudinal W bosons [12], treat W bosons as stable. In the above studies radiative corrections were not properly taken into account either.

In view of the achievable experimental precision, the theoretical predictions should include, however, both radiative corrections and the decays of the W bosons, i.e., the full process $\gamma\gamma \to 4f$ should be considered. The lowest-order amplitudes to the processes $\gamma\gamma \to 4f$ include diagrams with two resonant W bosons ("signal diagrams") as well as diagrams with only one or no W-resonance ("background diagrams"). Compared to the doubly-resonant diagrams, such singly-resonant and non-resonant diagrams are suppressed by roughly a factor Γ_W/M_W and $(\Gamma_W/M_W)^2$, respectively. On the other hand, radiative corrections modify the theoretical predictions by contributions of $\mathcal{O}(\alpha)$. Since Γ_W/M_W is also of $\mathcal{O}(\alpha)$, both the off-shell effects and the radiative corrections contribute to the $\gamma\gamma \to WW \to 4f$

[1] The corresponding FORTRAN code can be obtained from the authors upon request.

cross section in the same perturbative order. Hence, it is a promising approach to calculate the lowest-order matrix elements to the full $\gamma\gamma \to 4f$ process and take into account only the doubly-resonant part of the $\mathcal{O}(\alpha)$ corrections to the reaction $\gamma\gamma \to WW \to 4f$. This approach is known as double-pole approximation (DPA) where only the leading terms in the expansion of the amplitude around the poles of the resonant W propagators are included in the calculation. The overall accuracy is then $\mathcal{O}(\alpha)$ relative to the lowest-order prediction for the doubly-resonant W-pair signal. This approach has been described in [13] in some detail and successfully applied to W-pair production in e^+e^- annihilation in different versions [14–18].

The doubly-resonant virtual corrections consist of factorizable and non-factorizable contributions. The former comprise the corrections to on-shell W-pair production [19–21][2] and the decay of on-shell W bosons [23], the latter account for soft-photon exchange between the production and decay subprocesses [24]. Although the basic building blocks for the virtual corrections exist in the literature, the combination into a complete set of $\mathcal{O}(\alpha)$ corrections in DPA has not been done yet. The evaluation of bremsstrahlung processes $\gamma\gamma \to 4f + \gamma$ considered in this work serves as a further building block for the $\mathcal{O}(\alpha)$ corrections in DPA.

The calculation of lowest-order predictions for the processes $\gamma\gamma \to 4f$ and $\gamma\gamma \to 4f\gamma$ described in this paper closely follows the approach of [16] for the e^+e^- case. Fermion masses are neglected everywhere assuming that all mass singularities are avoided by phase-space cuts. Following [16] we construct an event generator based on multichannel Monte Carlo integration [25] using adaptive self-optimization [26]. A realistic photon spectrum can optionally be included in the parametrization of CompAZ [27] which is based on the results of [28]. In addition to the pure SM case, we calculate also the lowest-order matrix elements including anomalous couplings. Specifically, we consider ATGC [29,30] corresponding to $\mathrm{SU}(2)\times\mathrm{U}(1)$-gauge-invariant dimension-6 operators and genuine AQGC [31,32] which respect electromagnetic gauge-invariance and custodial $\mathrm{SU}(2)_\mathrm{c}$ symmetry. Finally, we include an effective $\gamma\gamma H$ coupling in our analysis in order to study the Higgs resonance in the reaction $\gamma\gamma \to H \to WW/ZZ \to 4f$.

The performance of the Monte Carlo generator is illustrated in a detailed numerical discussion. We present a survey of cross sections for a set of representative $4f$ and $4f\gamma$ final states and compare them with results obtained by the combination of the programs Whizard [33] version 1.28 and Madgraph [34]. We find agreement within statistical uncertainties. Moreover, we discuss some invariant-mass, energy, and angular distributions. We illustrate the impact of the realistic beam spectrum on cross sections and distributions, and study the size of various contributions to cross sections, such as from weak charged- or neutral-current, or from strong interactions. In view of the aimed precision calculation for $\gamma\gamma \to WW \to 4f(\gamma)$, which will include radiative corrections in DPA, we elaborate on the possibility to define a proper W-pair production signal. In this context, we investigate a naive signal definition which is based on doubly-resonant diagrams only and thus violates gauge invariance. We find that this naive definition, which works well for the e^+e^- case (cf. discussion of the so-called "CC03" cross section in [35]), is not satisfactory for $\gamma\gamma \to WW \to 4f$, but requires a proper gauge-invariant definition of the residue on the double resonance. For some $\gamma\gamma \to 4f$ and $\gamma\gamma \to 4f\gamma$ processes we investigate the effects of gauge-invariance violation by introducing gauge-boson decay widths. To this end, we compare results obtained with the naive introduction of constant or running widths with the gauge-invariant result obtained with the so-called "complex-mass scheme" [16]. Finally, we discuss the effects of ATGC and AQGC on cross sections. In particular, we estimate the bounds on anomalous couplings that could be set by a $\gamma\gamma$ collider, by assuming a photon spectrum and luminosities expected for the $\gamma\gamma$ option at TESLA.

This paper is organized as follows. In Sect. 2 we describe the calculation of the helicity amplitudes in the SM and give explicit results for $\gamma\gamma \to 4f$. In Sects. 3 and 4 we describe the calculation of the amplitudes with anomalous gauge-boson couplings and an effective $\gamma\gamma H$ interaction. Section 5 provides some details about the numerical Monte Carlo integration. In Sect. 6 we present the numerical results as outlined above. Our summary is given in Sect. 7.

2 Analytical results for amplitudes in the standard model

2.1 Notation and conventions

We consider reactions of the types

$$\begin{aligned}&\gamma(k_1,\lambda_1)+\gamma(k_2,\lambda_2) \qquad (2.1)\\ &\to f_1(p_1,\sigma_1)+\bar{f}_2(p_2,\sigma_2)+f_3(p_3,\sigma_3)+\bar{f}_4(p_4,\sigma_4),\\ &\gamma(k_1,\lambda_1)+\gamma(k_2,\lambda_2)\\ &\to f_1(p_1,\sigma_1)+\bar{f}_2(p_2,\sigma_2)+f_3(p_3,\sigma_3)+\bar{f}_4(p_4,\sigma_4)\\ &\qquad +\gamma(p_5,\sigma_5). \qquad (2.2)\end{aligned}$$

The arguments label the momenta k_i, p_j and helicities λ_k, σ_l (which take the values $\pm 1/2$ in the case of fermions and ± 1 in the case of photons) of the corresponding particles. We often use only the signs to denote the helicities. The fermion masses are neglected everywhere.

For the Feynman rules we follow the conventions of [36]. We extend the usual linear gauge-fixing term in the 't Hooft–Feynman gauge by a non-linear part according to [16,20,37] such that the vertex $\gamma W\phi$ vanishes, where ϕ are the would-be Goldstone bosons corresponding to the W bosons. Note that this also affects the gauge-boson couplings $\gamma\gamma WW$ and γWW. The corresponding Feynman rules relevant for $\gamma\gamma \to 4f(\gamma)$ in lowest order can be found in [16]. Since we neglect fermion masses, the would-be Goldstone bosons do not couple to fermions and do not occur in the Feynman graphs of the SM amplitudes to $\gamma\gamma \to 4f(\gamma)$, which leads to a considerable reduction of the number of Feynman diagrams.

[2] Radiative corrections to on-shell W-pair production, $\gamma\gamma \to WW$, were also considered in [22].

2.2 Classification of final states for $\gamma\gamma \to 4f(\gamma)$

The final states for $\gamma\gamma \to 4f$ and $\gamma\gamma \to 4f\gamma$ can be classified similarly to the processes $e^+e^- \to 4f$ and $e^+e^- \to 4f\gamma$ [16]. In the following, f and F are different fermions ($f \neq F$), and f' and F' denote their weak-isospin partners, respectively. We distinguish between states that are produced via charged-current (CC), via neutral-current (NC) interactions, or via both interaction types:

(i) CC reactions:
$\gamma\gamma \to f\bar{f}'F\bar{F}'$ (*CC31* family),

(ii) NC reactions:
(a) $\gamma\gamma \to f\bar{f}F\bar{F}$ (*NC40* family),
(b) $\gamma\gamma \to f\bar{f}f\bar{f}$ (*NC2·40* family),

(iii) Mixed CC/NC reactions:
$\gamma\gamma \to f\bar{f}f'\bar{f}'$ (*mix71* family).

The radiation of an additional photon does not change this classification. Following [38] we give the names of the process families in parentheses where the numbers correspond to the number of Feynman diagrams involved in unitary or non-linear gauge (for processes without neutrinos in the final state, not counting gluon-exchange diagrams).

Since the matrix elements depend on the colour structure of the final state we further distinguish between leptonic, semi-leptonic, and hadronic final states. Keeping in mind that we neglect fermion masses, omitting four-neutrino final states, and suppressing reactions that are equivalent by CP symmetry we end up with 17 different representative processes which we have listed in Table 1.

Since the photons are polarized after Compton backscattering, final states that are flavour equivalent up to a CP transformation need not necessarily yield the same cross section if the convolution over a realistic photon beam spectrum is included. However, as we neglect fermion masses, this is only relevant for the semi-leptonic CC processes $\gamma\gamma \to e^-\bar{\nu}_e u\bar{d}(\gamma)$ and $\gamma\gamma \to \nu_e e^+ d\bar{u}(\gamma)$.

Table 1. Set of representative processes for $\gamma\gamma \to 4f(\gamma)$

Final state	Reaction type	$\gamma\gamma \to$
leptonic	CC	$e^-\bar{\nu}_e\nu_\mu\mu^+$
	NC(a)	$e^-e^+\nu_\mu\bar{\nu}_\mu$
		$e^-e^+\mu^-\mu^+$
	NC(b)	$e^-e^+e^-e^+$
	CC/NC	$e^-e^+\nu_e\bar{\nu}_e$
semi-leptonic	CC(c)	$e^-\bar{\nu}_e u\bar{d}$
	NC(a)	$\nu_e\bar{\nu}_e u\bar{u}$
		$\nu_e\bar{\nu}_e d\bar{d}$
		$e^-e^+u\bar{u}$
		$e^-e^+d\bar{d}$
hadronic	CC	$u\bar{d}s\bar{c}$
	NC(a)	$u\bar{u}c\bar{c}$
	NC(a)	$u\bar{u}s\bar{s}$
	NC(a)	$d\bar{d}s\bar{s}$
	NC(b)	$u\bar{u}u\bar{u}$
	NC(b)	$d\bar{d}d\bar{d}$
	CC/NC	$u\bar{u}d\bar{d}$

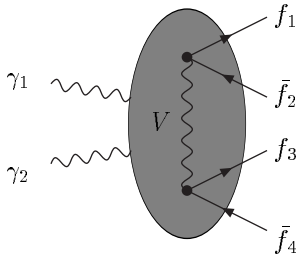

Fig. 1. Generic diagram for the process $\gamma\gamma \to 4f$ where the photons γ_1, γ_2 couple to the fermions $f_1, \ldots, \bar{f}_4$ and the gauge boson V in all possible ways

2.3 Lowest-order amplitudes for $\gamma\gamma \to 4f$

2.3.1 Construction of matrix elements

The amplitudes for the processes $\gamma\gamma \to 4f$ are constructed by attaching the two incoming photons in all possible ways to the corresponding diagrams with four external fermions as shown in Fig. 1. The matrix element of the generic diagram in Fig. 1, where two fermion lines are linked by a gauge boson V, can be written as

$$\begin{aligned}&\mathcal{M}^{\sigma_1\sigma_2\sigma_3\sigma_4}_{\lambda_1\lambda_2,V}(k_i,p_j,Q_j) \\ &= 4e^4\delta_{\sigma_1,-\sigma_2}\delta_{\sigma_3,-\sigma_4}\, g^{\sigma_1}_{V\bar{f}_1f_2} g^{\sigma_3}_{V\bar{f}_3f_4} A^{\sigma_1\sigma_3}_{\lambda_1\lambda_2,V}(k_i,p_j,Q_j),\end{aligned} \tag{2.3}$$

where k_i, p_j and Q_j ($i = 1,2; j = 1,\ldots,4$) stand for the momenta and relative electric charges of the particles, respectively. The coupling factors (relative to the electric unit charge e) read

$$\begin{aligned} g^{\sigma}_{\gamma\bar{f}_if_i} &= -Q_i, \\ g^{\sigma}_{Z\bar{f}_if_i} &= -\frac{s_\mathrm{w}}{c_\mathrm{w}}Q_i + \frac{I^3_{\mathrm{w},i}}{c_\mathrm{w}s_\mathrm{w}}\delta_{\sigma-}, \\ g^{\sigma}_{W\bar{f}_if'_i} &= \frac{1}{\sqrt{2}s_\mathrm{w}}\delta_{\sigma-}, \quad g^{\sigma}_{g\bar{f}_if_i} = \frac{g_\mathrm{s}}{e}, \end{aligned} \tag{2.4}$$

where $I^3_{\mathrm{w},i} = \pm 1/2$ denotes the weak isospin of the fermion f_i and g_s the strong coupling constant. The weak mixing angle is defined by

$$\cos\theta_\mathrm{w} = c_\mathrm{w} = \frac{M_W}{M_Z}, \qquad s_\mathrm{w} = \sqrt{1-c^2_\mathrm{w}}. \tag{2.5}$$

Quark mixing is neglected everywhere, i.e. we set the CKM matrix equal to the unit matrix. The auxiliary functions $A^{\sigma_1\sigma_3}_{\lambda_1\lambda_2,V}$ are calculated within the Weyl–van der Waerden (WvdW) formalism following the conventions of [39]. The WvdW spinor products are defined by

$$\begin{aligned}&\langle pq\rangle = \epsilon^{AB}p_Aq_B \\ &= 2\sqrt{p_0q_0}\left(\mathrm{e}^{-\mathrm{i}\phi_p}\cos\frac{\theta_p}{2}\sin\frac{\theta_q}{2} - \mathrm{e}^{-\mathrm{i}\phi_q}\cos\frac{\theta_q}{2}\sin\frac{\theta_p}{2}\right),\end{aligned} \tag{2.6}$$

where p_A, q_A are the associated momentum spinors for the momenta

$$p^\mu = p_0(1, \sin\theta_p\cos\phi_p, \sin\theta_p\sin\phi_p, \cos\theta_p),$$
$$q^\mu = q_0(1, \sin\theta_q\cos\phi_q, \sin\theta_q\sin\phi_q, \cos\theta_q). \quad (2.7)$$

Moreover, we define the shorthands

$$\begin{aligned}\langle p_i P_k p_j\rangle &= p_{i,\dot{A}} P_k^{\dot{A}B} p_{j,B} = p_{i,\dot{A}} p_k^{\dot{A}} p_k^B p_{j,B}\\ &= \langle p_i p_k\rangle^* \langle p_j p_k\rangle,\\ \langle p_i[P_l + P_m]p_j\rangle &= \langle p_i P_l p_j\rangle + \langle p_i P_m p_j\rangle, \end{aligned} \quad (2.8)$$

where $p_{k,l,m}$ are light-like momenta, i.e., $p_k^2 = p_l^2 = p_m^2 = 0$. In the following, the denominators of the gauge-boson propagators are abbreviated by

$$P_V(p) = \frac{1}{p^2 - M_V^2}, \quad V = \gamma, Z, W, g, \quad M_\gamma = M_g = 0. \quad (2.9)$$

The introduction of the finite width is described in Sect. 2.4 below.

The auxiliary functions $A^{\sigma_1\sigma_3}_{\lambda_1\lambda_2,V}$ explicitly read

$$\begin{aligned}
&A^{--}_{++,V}(k_i,p_j,Q_j) = (\langle p_2 p_4\rangle^*)^2\\
&\times\Bigg\{-Q_1^2\frac{\langle p_1p_2\rangle^*\langle p_3p_4\rangle P_V(p_3+p_4)}{\langle k_1p_1\rangle^*\langle k_1p_2\rangle^*\langle k_2p_1\rangle^*\langle k_2p_2\rangle^*}\\
&-Q_1Q_3\frac{(p_1+p_2-k_1)^2P_V(p_1+p_2-k_1)}{\langle k_1p_1\rangle^*\langle k_1p_2\rangle^*\langle k_2p_3\rangle^*\langle k_2p_4\rangle^*}\\
&+Q_3(Q_1-Q_2)P_V(p_1+p_2)\times\\
&\Bigg[\frac{-\langle p_2p_4\rangle^*\langle p_1p_2\rangle + \langle k_1p_4\rangle^*\langle k_1p_1\rangle M_V^2 P_V(p_1+p_2-k_1)}{\langle k_1p_2\rangle^*\langle k_1p_4\rangle^*\langle k_2p_3\rangle^*\langle k_2p_4\rangle^*}\\
&\quad+(k_1\leftrightarrow k_2)\Bigg]\\
&+(Q_1-Q_2)^2P_V(p_1+p_2)P_V(p_3+p_4)\\
&\times\Bigg[-\langle p_2p_4\rangle^*\frac{\langle p_2p_4\rangle^*\langle p_1p_2\rangle\langle p_3p_4\rangle + M_V^2\langle p_1p_3\rangle}{2\langle k_1p_2\rangle^*\langle k_1p_4\rangle^*\langle k_2p_2\rangle^*\langle k_2p_4\rangle^*}\\
&+M_V^2P_V(p_1+p_2-k_1)\frac{\langle k_1p_1\rangle\langle k_2p_3\rangle}{\langle k_1p_2\rangle^*\langle k_2p_4\rangle^*}\Bigg]\\
&+(\{p_1,Q_1;p_2,Q_2\}\leftrightarrow\{p_3,Q_3;p_4,Q_4\})\Bigg\},
\end{aligned}$$

$$\begin{aligned}
&A^{--}_{+-,V}(k_i,p_j,Q_j)\\
&= Q_1^2P_V(p_3+p_4)\frac{\langle p_2p_4\rangle^*\langle k_1p_1\rangle\langle k_2[P_2+P_4]p_3\rangle}{\langle k_1p_1\rangle^*\langle k_2p_1\rangle(p_2+p_3+p_4)^2}\\
&+Q_2^2P_V(p_3+p_4)\frac{\langle k_2p_2\rangle^*\langle p_1p_3\rangle\langle p_4[P_1+P_3]k_1\rangle}{\langle k_1p_2\rangle^*\langle k_2p_2\rangle(p_1+p_3+p_4)^2}\\
&+Q_1Q_2P_V(p_3+p_4)\frac{\langle p_2[K_1-P_1]p_3\rangle\langle p_4[K_1-P_3]p_1\rangle}{\langle k_1p_1\rangle^*\langle k_1p_2\rangle^*\langle k_2p_1\rangle\langle k_2p_2\rangle}\\
&+(Q_2-Q_1)P_V(p_3+p_4)\frac{\langle p_2p_4\rangle^*\langle p_1p_3\rangle}{\langle k_1p_2\rangle^*\langle k_2p_1\rangle}\\
&\times\Bigg[Q_2\frac{\langle p_4[K_1-P_3]p_1\rangle}{\langle k_1p_4\rangle^*\langle k_2p_2\rangle} + Q_1\frac{\langle p_2[K_1-P_1]p_3\rangle}{\langle k_1p_1\rangle^*\langle k_2p_3\rangle}\Bigg]\\
&+\frac{1}{2}(Q_2-Q_1)^2P_V(p_1+p_2)P_V(p_3+p_4)\\
&\times\langle p_2p_4\rangle^*\langle p_1p_3\rangle\times\\
&\frac{\langle p_2[K_1-P_1]p_3\rangle\langle p_4[K_1-P_3]p_1\rangle - M_V^2\langle p_2p_4\rangle^*\langle p_1p_3\rangle}{\langle k_1p_2\rangle^*\langle k_1p_4\rangle^*\langle k_2p_1\rangle\langle k_2p_3\rangle}\\
&+[-Q_1+(Q_1-Q_2)2(k_1p_1)P_V(p_1+p_2)]\\
&\times[Q_4+(Q_3-Q_4)2(k_2p_4)P_V(p_3+p_4)]\\
&\times\frac{(\langle p_2[K_1-P_1]p_3\rangle)^2P_V(p_1+p_2-k_1)}{\langle k_1p_1\rangle^*\langle k_1p_2\rangle^*\langle k_2p_3\rangle\langle k_2p_4\rangle}\\
&+(\{p_1,Q_1;p_2,Q_2\}\leftrightarrow\{p_3,Q_3;p_4,Q_4\}). \quad (2.10)
\end{aligned}$$

The other auxiliary functions $A^{\sigma_1\sigma_3}_{\lambda_1\lambda_2,V}$ follow from the relations

$$\begin{aligned}
&A^{-\sigma_1,\sigma_3}_{\lambda_1\lambda_2,V}(k_i,p_j,Q_j)\\
&= \Big[A^{\sigma_1\sigma_3}_{\lambda_1\lambda_2,V}(k_i,p_j,Q_j)\Big]_{\{p_1,Q_1\}\leftrightarrow\{p_2,-Q_2\}},\\
&A^{\sigma_1,-\sigma_3}_{\lambda_1\lambda_2,V}(k_i,p_j,Q_j)\\
&= \Big[A^{\sigma_1\sigma_3}_{\lambda_1\lambda_2,V}(k_i,p_j,Q_j)\Big]_{\{p_3,Q_3\}\leftrightarrow\{p_4,-Q_4\}} \quad (2.11)
\end{aligned}$$

and

$$A^{-\sigma_1,-\sigma_3}_{-\lambda_1,-\lambda_2,V}(k_i,p_j,Q_j) = \Big[A^{\sigma_1\sigma_3}_{\lambda_1\lambda_2,V}(k_i,p_j,Q_j)\Big]^*. \quad (2.12)$$

The last relation expresses a parity transformation. Note that the operation of complex conjugation in (2.12) must not affect the gauge-boson widths in the propagator functions P_V which will be introduced in Sect. 2.4.

The calculation of the helicity amplitudes for $\gamma\gamma \to 4f\gamma$ proceeds along the same lines. The result, however, is quite lengthy so that we do not write it down explicitly.

2.3.2 Squared amplitudes for leptonic and semi-leptonic final states

The result for leptonic and semi-leptonic final states follows immediately from the generic amplitude (2.3). The gauge boson cannot be a gluon in this case, and the sum over the colour degrees of freedom in the squared matrix elements trivially leads to the global factors $N^{\mathrm{c}}_{\mathrm{lept}} = 1$ and $N^{\mathrm{c}}_{\mathrm{semilept}} = 3$. Note that for NC diagrams the result for the amplitude is much simpler than for CC diagrams, since all terms in (2.10) involving a factor $(Q_1 - Q_2)$ or $(Q_3 - Q_4)$ drop out. Most of these terms originate from diagrams where a photon couples to a virtual W boson.

The explicit results for the colour-summed squared matrix elements read

$$\sum_{\text{colour}} |\mathcal{M}_{\text{CC}}|^2 = N^{\text{c}} |\mathcal{M}_W|^2, \tag{2.13}$$

$$\sum_{\text{colour}} |\mathcal{M}_{\text{NC(a)}}|^2 = N^{\text{c}} \left|\mathcal{M}_{\text{NC}}\right|^2, \tag{2.14}$$

$$\sum_{\text{colour}} |\mathcal{M}_{\text{NC(b)}}|^2 = N^{\text{c}} \left|\mathcal{M}_{\text{NC}} - [\mathcal{M}_{\text{NC}}]_{\{p_1,Q_1,\sigma_1\}\leftrightarrow\{p_3,Q_3,\sigma_3\}}\right|^2, \tag{2.15}$$

$$\sum_{\text{colour}} |\mathcal{M}_{\text{CC/NC}}|^2 = N^{\text{c}} \left|\mathcal{M}_{\text{NC}} - [\mathcal{M}_W]_{\{p_1,Q_1,\sigma_1\}\leftrightarrow\{p_3,Q_3,\sigma_3\}}\right|^2, \tag{2.16}$$

where we use the shorthand

$$\mathcal{M}_{\text{NC}} = \sum_{V=\gamma,Z} \mathcal{M}_V \tag{2.17}$$

and suppress the helicity indices and the dependence on momenta and relative charges. The relative signs account for interchanging external fermion lines.

2.3.3 Squared amplitudes for hadronic final states

Next we consider purely hadronic final states, i.e., the cases where all final-state fermions are quarks. This renders the summation of the squared matrix elements over the colour degrees of freedom non-trivial, and in addition gluon-exchange diagrams appear. Since gluon-exchange diagrams require two quark–anti-quark pairs in the final state they do not appear in CC processes. For CC processes there is only one possibility for the colour flow, and the summation over the colour degrees of freedom leads to an overall factor $N^{\text{c}}_{\text{had,CC}} = 3^2 = 9$ to the squared matrix elements as given in (2.13).

For NC reactions we have to compute the sum of pure electroweak (ew) and gluon-exchange (QCD) matrix elements,

$$\mathcal{M}^{c_1c_2c_3c_4}_{\text{had}} = \mathcal{M}^{c_1c_2c_3c_4}_{\text{had,ew}} + \mathcal{M}^{c_1c_2c_3c_4}_{\text{had,QCD}}, \tag{2.18}$$

where c_i denotes the colour indices of the quarks. The electroweak diagrams are diagonal in colour space and therefore read

$$\begin{aligned}
\mathcal{M}^{c_1c_2c_3c_4}_{\text{NC(a),had,ew}} &= \mathcal{M}_{\text{NC}} \delta_{c_1c_2}\delta_{c_3c_4}, \\
\mathcal{M}^{c_1c_2c_3c_4}_{\text{NC(b),had,ew}} &= \mathcal{M}_{\text{NC}} \delta_{c_1c_2}\delta_{c_3c_4} \\
&\quad - [\mathcal{M}_{\text{NC}}]_{\{p_1,Q_1,\sigma_1\}\leftrightarrow\{p_3,Q_3,\sigma_3\}}\ \delta_{c_3c_2}\delta_{c_1c_4}.
\end{aligned} \tag{2.19}$$

The gluon-exchange diagrams are obtained from the generic formula (2.3) by inserting the corresponding generators, $\lambda^a/2$, of the gauge group SU(3),

$$\begin{aligned}
\mathcal{M}^{c_1c_2c_3c_4}_{\text{NC(a),had,QCD}} &= \mathcal{M}_g \frac{1}{4}\lambda^a_{c_1c_2}\lambda^a_{c_3c_4}, \\
\mathcal{M}^{c_1c_2c_3c_4}_{\text{NC(b),had,QCD}} &= \mathcal{M}_g \frac{1}{4}\lambda^a_{c_1c_2}\lambda^a_{c_3c_4} \\
&\quad - [\mathcal{M}_g]_{\{p_1,Q_1,\sigma_1\}\leftrightarrow\{p_3,Q_3,\sigma_3\}}\ \frac{1}{4}\lambda^a_{c_3c_2}\lambda^a_{c_1c_4}.
\end{aligned} \tag{2.20}$$

The matrix element $\mathcal{M}_g$ is defined by (2.3) with $V = g$.

Carrying out the colour sum using the completeness relation for the Gell-Mann matrices,

$$\lambda^a_{ij}\lambda^a_{kl} = -\frac{2}{3}\delta_{ij}\delta_{kl} + 2\delta_{il}\delta_{jk}, \tag{2.21}$$

yields

$$\begin{aligned}
&\sum_{\text{colour}} |\mathcal{M}_{\text{NC(a),had}}|^2 = 9|\mathcal{M}_{\text{NC}}|^2 + 2|\mathcal{M}_g|^2, \\
&\sum_{\text{colour}} |\mathcal{M}_{\text{NC(b),had}}|^2 = 9|\mathcal{M}_{\text{NC}}|^2 \\
&\quad +9\left|[\mathcal{M}_{\text{NC}}]_{\{p_1,Q_1,\sigma_1\}\leftrightarrow\{p_3,Q_3,\sigma_3\}}\right|^2 + 2|\mathcal{M}_g|^2 \\
&\quad +2\left|[\mathcal{M}_g]_{\{p_1,Q_1,\sigma_1\}\leftrightarrow\{p_3,Q_3,\sigma_3\}}\right|^2 \\
&\quad -6\,\text{Re}\left\{\mathcal{M}_{\text{NC}}\,[\mathcal{M}^*_{\text{NC}}]_{\{p_1,Q_1,\sigma_1\}\leftrightarrow\{p_3,Q_3,\sigma_3\}}\right\} \\
&\quad +\frac{4}{3}\,\text{Re}\left\{\mathcal{M}_g\,[\mathcal{M}^*_g]_{\{p_1,Q_1,\sigma_1\}\leftrightarrow\{p_3,Q_3,\sigma_3\}}\right\} \\
&\quad -8\,\text{Re}\left\{\mathcal{M}_{\text{NC}}\,[\mathcal{M}^*_g]_{\{p_1,Q_1,\sigma_1\}\leftrightarrow\{p_3,Q_3,\sigma_3\}}\right\} \\
&\quad -8\,\text{Re}\left\{\mathcal{M}_g\,[\mathcal{M}^*_{\text{NC}}]_{\{p_1,Q_1,\sigma_1\}\leftrightarrow\{p_3,Q_3,\sigma_3\}}\right\}.
\end{aligned} \tag{2.22}$$

All squared matrix elements of this section have been numerically compared with results obtained with the program Madgraph [34] at several phase-space points, and perfect agreement has been found.

2.4 Implementation of finite gauge-boson widths

We have implemented the finite widths of the W- and Z-boson propagators[3] in four different ways:
(1) *fixed width* in all propagators:

$$P_V(p) = \frac{1}{p^2 - M_V^2 + \text{i}M_V\Gamma_V}, \tag{2.23}$$

(2) *step width* (fixed width in time-like propagators):

$$P_V(p) = \frac{1}{p^2 - M_V^2 + \text{i}M_V\Gamma_V\theta(p^2)}, \tag{2.24}$$

[3] We have also supplemented the explicit gauge-boson masses appearing in the numerators of (2.10) by the corresponding widths, because these mass terms originate from denominators upon combining different diagrams.

(3) *running width* in time-like propagators:

$$P_V(p) = \frac{1}{p^2 - M_V^2 + \mathrm{i}p^2(\Gamma_V/M_V)\theta(p^2)}, \tag{2.25}$$

(4) *complex-mass scheme* [16]: complex gauge-boson masses are used everywhere, i.e. $\sqrt{M_V^2 - \mathrm{i}M_V\Gamma_V}$ instead of M_V in all propagators and couplings. This results in a constant width in all propagators,

$$P_V(p) = \frac{1}{p^2 - M_V^2 + \mathrm{i}M_V\Gamma_V}, \tag{2.26}$$

and in a complex weak mixing angle

$$c_\mathrm{w}^2 = 1 - s_\mathrm{w}^2 = \frac{M_W^2 - \mathrm{i}M_W\Gamma_W}{M_Z^2 - \mathrm{i}M_Z\Gamma_Z}. \tag{2.27}$$

The virtues and drawbacks of the first three schemes are discussed in [40]. All but the complex-mass scheme, in general, violate SU(2) gauge invariance; the step- and the running-width schemes also violate electromagnetic $\mathrm{U}(1)_\mathrm{em}$ gauge invariance, which is preserved by using a fixed width. As known from many examples in e^+e^- physics [16,40,41], gauge-invariance-violating effects, in particular when enhanced by factors p^2/M_V^2 as in the running-width scheme, can lead to totally wrong results. Furthermore, the violation of $\mathrm{U}(1)_\mathrm{em}$ gauge invariance also causes a dependence of matrix elements and cross sections on the gauge chosen for external photons. In $e^+e^- \to 4f$ and $e^+e^- \to 6f$ this problem does not occur since no external photons are involved.

The complex-mass scheme, which was introduced in [16] for tree-level calculations, preserves gauge invariance and thus all Ward identities which rule gauge cancellations. Its application is particularly simple for $\gamma\gamma \to 4f(\gamma)$ in the non-linear gauge. In this case, no couplings involving explicit gauge-boson masses appear, and it is sufficient to introduce the finite gauge-boson widths in the propagators [cf. (2.26)] and to introduce the complex weak mixing angle (2.27) in the couplings.

For CC processes $\gamma\gamma \to 4f(\gamma)$ with massless fermions, the fixed-width (FW) approach in the non-linear gauge and the complex-mass scheme (CMS) are practically equivalent, because all Feynman graphs are proportional to e^4/s_w^2 (e^5/s_w^2) and gauge-boson masses appear only in propagator denominators. In this case the corresponding amplitudes in the two schemes differ only in the global factor $s_{\mathrm{w,FW}}^2/s_{\mathrm{w,CMS}}^2$, where $s_{\mathrm{w,FW}}$ and $s_{\mathrm{w,CMS}}$ are the values of s_w in the different schemes, i.e., $s_{\mathrm{w,FW}}$ is derived from the ratio of real gauge-boson masses and $s_{\mathrm{w,CMS}}$ from complex masses. Thus, both squared amplitudes are gauge invariant and are equal up to the factor $|s_{\mathrm{w,FW}}/s_{\mathrm{w,CMS}}|^4$ which is equal to 1 up to terms of $\mathcal{O}(\Gamma_W^2/M_W^2)$.

For NC and CC/NC processes a similar reasoning can be used to show that the fixed-width approach does not violate gauge invariance in $\gamma\gamma \to 4f(\gamma)$ for massless fermions. The trick is to apply the above argument to gauge-invariant subsets of diagrams. For NC diagrams with photon exchange, which is the (gauge-invariant) QED subset of diagrams (Fig. 1 with $V = \gamma$), there is nothing to show. The sum of NC diagrams of type NC(a) with Z-boson exchange (Fig. 1 with $V = Z$) again involves c_w and s_w only in a global coupling factor (per helicity channel); the remaining dependence on the gauge-boson masses is located in the propagator denominators. Thus, the subamplitudes of the fixed-width and the complex-mass scheme are again identical up to a global factor and both preserve gauge invariance and Ward identities. For NC processes of type NC(b) a second class of diagrams exists (Fig. 1 with $V = \gamma, Z$ and external fermions interchanged). This new class of diagrams forms a gauge-invariant subset because of the different flow of fermion numbers. Thus, the reasoning for type NC(a) applies to both classes of diagrams of NC(b) reactions. The same argument is also valid for the subset of CC diagrams in mixed CC/NC reactions.

In summary, we have argued that the use of naive fixed gauge-boson widths does not lead to gauge-invariance violations in amplitudes for $\gamma\gamma \to 4f(\gamma)$ as long as fermions are massless and the non-linear gauge with vanishing $\gamma W\phi$ coupling (or the complex W boson mass in this coupling if the 't Hooft–Feynman gauge is chosen) is used. The corresponding squared amplitudes agree with the ones of the (gauge-invariant) complex-mass scheme up to terms of $\mathcal{O}(\Gamma_W/M_W)$, for CC processes even up to terms of $\mathcal{O}(\Gamma_W^2/M_W^2)$.

2.5 W-pair signal diagrams and double-pole approximation

The diagrams to CC and CC/NC processes comprise graphs with two, one, or no internal W boson lines that can become resonant, similar to the situation for $e^+e^- \to WW \to 4f$ (see [35,42] and references therein). It is interesting to investigate the possibility to define an amplitude for the W-pair signal based on doubly-resonant contributions only, because such an amplitude is much simpler than the full amplitudes for four-fermion production and is universal (up to colour factors) for all relevant $4f$ final states. Moreover, this study is an important exercise for the calculation of radiative corrections to $\gamma\gamma \to WW \to 4f$ in the so-called double-pole approximation (DPA), where only doubly-resonant contributions are taken into account. Taking simply all doubly-resonant diagrams, of course, yields a result that is not gauge invariant. Nevertheless in the e^+e^- case the lowest-order cross section based on such a gauge-dependent amplitude (defined in the 't Hooft–Feynman gauge), known as "CC03 cross section", is a very useful quantity that is very close to the full $4f$ calculation if both W bosons are close to resonance. The CC03 amplitude can be rendered gauge invariant upon deforming the momenta of the four outgoing fermions in such a way that the intermediate W boson states become on shell, because the residues of the W-resonances are gauge-invariant quantities. This "on-shell projection", which is part of the DPA, involves some freedom, and different versions, which have been described in [15,17], differ by contributions of relative order $\mathcal{O}(\Gamma_W/M_W)$.

We want to perform the exercise to study the usefulness of a possible "CC03"[4] off-shell cross section for $\gamma\gamma \to WW \to 4f$. To this end, we define the amplitude for the off-shell W-pair signal by evaluating the three W-pair diagrams in the non-linear gauge with polarization vectors $\varepsilon_i(k_i)$ for the incoming photons, which obey the gauge conditions

$$\varepsilon_1(k_1)\cdot k_2 = \varepsilon_2(k_2)\cdot k_1 = 0. \tag{2.28}$$

In terms of WvdW spinors, this means that the gauge spinors g_1 and g_2 of the photons are identified with the spinors of the momenta k_2 and k_1, respectively. With this choice the auxiliary functions for the matrix elements (2.3) read

$$\begin{aligned}
&A^{--}_{++,WW}(k_i,p_j,Q_j)\\
&= P_W(p_1+p_2)P_W(p_3+p_4)\,\frac{\langle p_2p_4\rangle^*}{\langle k_1k_2\rangle^*}\\
&\quad\times\Bigg\{[P_W(p_1+p_2-k_1)]_{\Gamma_W=0}\\
&\quad\times\Bigg[\langle k_2p_1\rangle\langle k_2p_3\rangle\langle k_2[P_1+P_2]k_1\rangle\\
&\qquad+\langle k_1p_1\rangle\langle k_1p_3\rangle\langle k_1[P_3+P_4]k_2\rangle\\
&\qquad+\frac{\langle p_1p_3\rangle}{\langle k_1k_2\rangle^*}\langle k_2[P_1+P_2]k_1\rangle\langle k_1[P_3+P_4]k_2\rangle\\
&\qquad-2(k_1\cdot k_2)\langle k_1p_1\rangle\langle k_2p_3\rangle\Bigg]\\
&\qquad-\frac{1}{2}\langle p_1p_3\rangle\langle k_1k_2\rangle\Bigg\}+(k_1\leftrightarrow k_2),\\
&A^{--}_{+-,WW}(k_i,p_j,Q_j) = P_W(p_1+p_2)P_W(p_3+p_4)\\
&\quad\times[P_W(p_1+p_2-k_1)+P_W(p_1+p_2-k_2)]_{\Gamma_W=0}\\
&\quad\times\Bigg\{\langle k_2[P_1+P_2]k_1\rangle\\
&\quad\times\left[\frac{\langle k_2p_2\rangle^*\langle k_2p_4\rangle^*\langle p_1p_3\rangle}{\langle k_1k_2\rangle^*}-\frac{\langle p_2p_4\rangle^*\langle k_1p_1\rangle\langle k_1p_3\rangle}{\langle k_1k_2\rangle}\right]\\
&\quad-\frac{\langle p_2p_4\rangle^*\langle p_1p_3\rangle}{2(k_1k_2)}\langle k_2[P_1+P_2]k_1\rangle^2\\
&\qquad+\langle k_2p_2\rangle^*\langle k_2p_4\rangle^*\langle k_1p_1\rangle\langle k_1p_3\rangle\Bigg\}.
\end{aligned}\tag{2.29}$$

Note that the $A^{\sigma_1\sigma_3}_{\lambda_1\lambda_2,WW}$ do not coincide with the parts of the functions $A^{\sigma_1\sigma_3}_{\lambda_1\lambda_2,W}$ of (2.10) that are proportional to $P_W(p_1+p_2)P_W(p_3+p_4)$ because the derivation of (2.10) involves rearrangements of various singly-resonant contributions. We point out that the definition (2.29) is neither independent of the gauge fixing used to define gauge-boson propagators nor of the gauge of the external photons. The definition is gauge invariant after the outgoing fermion momenta p_i are on-shell projected as described above, while leaving the resonant propagators $P_W(p_1+p_2)P_W(p_3+p_4)$ untouched. This defines the lowest-order amplitude in DPA. Finally, we stress that the t- and u-channel W-propagators in (2.29) do not receive a finite W-width; otherwise the gauge invariance of the DPA would be spoiled.

[4] The name also fits to the $\gamma\gamma$ case where three W-pair diagrams exist in unitary or non-linear gauge.

3 Inclusion of anomalous gauge-boson couplings

In this section we introduce the most important anomalous gauge-boson couplings accessible by the process $\gamma\gamma \to 4f$ and give explicit analytical results for the corresponding helicity amplitudes.

3.1 The effective Lagrangians

First we consider anomalous triple gauge-boson couplings (ATGC) in the charged-current sector, i.e., anomalous γWW and the related $\gamma\gamma WW$ couplings. Instead of using rather general parametrizations of non-standard couplings [29], we follow the approach already used at LEP2 to reduce the number of free parameters by requiring that all symmetries of the SM are respected. From the resulting operators we only keep those that appear in the lowest-order cross section of $\gamma\gamma \to 4f$. Specifically, we start from the gauge-invariant CP-conserving effective Lagrangian with dimension-6 operators [30]

$$\begin{aligned}
\mathcal{L}^{\mathrm{ATGC}}_{\mathrm{CC}} &= \mathrm{i}g_1\frac{\alpha_{B\phi}}{M_W^2}\,(D_\mu\Phi)^\dagger B^{\mu\nu}(D_\nu\Phi)\\
&\quad-\mathrm{i}g_2\frac{\alpha_{W\phi}}{M_W^2}\,(D_\mu\Phi)^\dagger\boldsymbol{\sigma}\cdot\mathbf{W}^{\mu\nu}(D_\nu\Phi)\\
&\quad-g_2\frac{\alpha_W}{6M_W^2}\,\mathbf{W}^\mu{}_\nu\cdot(\mathbf{W}^\nu{}_\rho\times\mathbf{W}^\rho{}_\mu),
\end{aligned}\tag{3.1}$$

where Φ is the Higgs doublet field and

$$\begin{aligned}
B^{\mu\nu} &= \partial^\mu B^\nu-\partial^\nu B^\mu,\\
\mathbf{W}^{\mu\nu} &= (W_1^{\mu\nu},W_2^{\mu\nu},W_3^{\mu\nu})\\
&= \partial^\mu\mathbf{W}^\nu-\partial^\nu\mathbf{W}^\mu+g_2\mathbf{W}^\mu\times\mathbf{W}^\nu
\end{aligned}\tag{3.2}$$

are the field strengths of the U(1) and SU(2) gauge fields, respectively. The Pauli matrices are combined into the vector $\boldsymbol{\sigma}=(\sigma_1,\sigma_2,\sigma_3)$, and the parameters g_1, g_2 denote the gauge couplings.[5] Inserting the vacuum expectation value of the Higgs field Φ, we can relate the coefficients $\alpha_{B\phi}$, $\alpha_{W\phi}$, and α_W to the coefficients of the Lagrangian considered in the LEP2 analysis [30],

[5] In order to be compatible with the conventions of [36] used for the SM amplitudes above, we had to change the sign of the SU(2) coupling g_2 with respect to [30].

$$\Delta g_1^Z = \frac{\alpha_{W\phi}}{c_\mathrm{w}^2},$$

$$\Delta\kappa_\gamma = -\frac{c_\mathrm{w}^2}{s_\mathrm{w}^2}(\Delta\kappa_Z - \Delta g_1^Z) = \alpha_{W\phi} + \alpha_{B\phi},$$

$$\lambda_\gamma = \lambda_Z = \alpha_W. \tag{3.3}$$

In contrast to the pure anomalous γWW coupling [29], the SU(2)×U(1) symmetry of the effective Lagrangian (3.1) induces additional anomalous $\gamma\gamma WW$ and $\gamma W\phi$ couplings. The corresponding Feynman rules are

$$\begin{aligned}
&\mathrm{i}\Gamma^{\gamma W^+W^-}_{\mu\nu\rho}(k_0,k_+,k_-) = -\mathrm{i}e\,\{\Delta\kappa_\gamma(k_{0\nu}g_{\mu\rho} - k_{0\rho}g_{\mu\nu})\\
&\quad -\frac{\lambda_\gamma}{M_W^2}\,[k_{+\mu}k_{-\nu}k_{0\rho} - k_{-\mu}k_{+\rho}k_{0\nu}\\
&\quad +g_{\nu\rho}(k_{-\mu}(k_+k_0) - k_{+\mu}(k_-k_0))\\
&\quad +g_{\mu\rho}(k_{0\nu}(k_+k_-) - k_{-\nu}(k_+k_0))\\
&\quad +g_{\mu\nu}(k_{+\rho}(k_-k_0) - k_{0\rho}(k_+k_-))]\}\,,\\
&\mathrm{i}\Gamma^{\gamma\gamma W^+W^-}_{\mu\nu\rho\sigma}(k_1,k_2,k_+,k_-)\\
&= -\mathrm{i}e^2\frac{\lambda_\gamma}{M_W^2}\Big\{g_{\mu\nu}g_{\rho\sigma}(k_1+k_2)^2 + g_{\mu\rho}g_{\nu\sigma}(k_2k_+ + k_1k_-)\\
&\quad +g_{\nu\rho}g_{\mu\sigma}(k_1k_+ + k_2k_-)\\
&\quad +g_{\mu\nu}\,[(k_1+k_2)_\rho k_{+\sigma} + (k_1+k_2)_\sigma k_{-\rho}]\\
&\quad +g_{\rho\sigma}\,[(k_+ + k_-)_\mu k_{1\nu} + (k_+ + k_-)_\nu k_{2\mu}]\\
&\quad +g_{\mu\rho}\,[(k_1-k_2)_\sigma k_{+\nu} - k_{1\nu}k_{+\sigma} - k_{1\sigma}k_{-\nu}]\\
&\quad +g_{\mu\sigma}\,[(k_1-k_2)_\rho k_{-\nu} - k_{1\nu}k_{-\rho} - k_{1\rho}k_{+\nu}]\\
&\quad +g_{\nu\rho}\,[(k_2-k_1)_\sigma k_{+\mu} - k_{2\mu}k_{+\sigma} - k_{2\sigma}k_{-\mu}]\\
&\quad +g_{\nu\sigma}\,[(k_2-k_1)_\rho k_{-\mu} - k_{2\mu}k_{-\rho} - k_{2\rho}k_{+\mu}]\Big\},
\end{aligned} \tag{3.4}$$

$$\mathrm{i}\Gamma^{\gamma W\phi}_{\mu\nu}(k_0,k_W,k_\phi) = -\mathrm{i}e\frac{\Delta\kappa_\gamma}{M_W}\,\{(k_\phi k_0)g_{\mu\nu} - k_{\phi,\mu}k_{0,\nu}\}\,,$$

where all fields and momenta are considered incoming. Note that the neglect of the contribution to the quartic coupling $\gamma\gamma WW$, which is proportional to λ_γ, would lead to a violation of electromagnetic gauge invariance in predictions for $\gamma\gamma \to WW(\to 4f)$. In contrast, neglecting the $\gamma W\phi$ coupling, which is proportional to $\Delta\kappa_\gamma$, would not spoil the electromagnetic gauge invariance of the predictions.

Next we consider anomalous triple gauge-boson couplings involving only the neutral gauge bosons γ and Z. Assuming Lorentz invariance and electromagnetic gauge invariance, the most general effective dimension-6 Lagrangian for $\gamma\gamma Z$, γZZ, and ZZZ couplings can be written as [43][6]

$$\begin{aligned}
\mathcal{L}_\mathrm{NC}^\mathrm{ATGC} = \frac{e}{M_Z^2}\Big\{&\left[f_4^\gamma(\partial_\mu F^{\mu\nu}) - f_4^Z(\partial_\mu Z^{\mu\nu})\right] Z_{\nu\rho}Z^\rho\\
&+\left[f_5^\gamma(\partial_\mu F^{\mu\nu}) - f_5^Z(\partial_\mu Z^{\mu\nu})\right] \tilde{Z}_{\nu\rho}Z^\rho\\
&+\left[h_1^\gamma(\partial_\mu F^{\mu\nu}) - h_1^Z(\partial_\mu Z^{\mu\nu})\right] F_{\nu\rho}Z^\rho\\
&+\left[h_3^\gamma(\partial_\mu F^{\mu\nu}) - h_3^Z(\partial_\mu Z^{\mu\nu})\right] \tilde{F}_{\nu\rho}Z^\rho\Big\},
\end{aligned} \tag{3.5}$$

with the abelian field-strength tensors

$$F^{\mu\nu} = \partial^\mu A^\nu - \partial^\nu A^\mu, \qquad Z^{\mu\nu} = \partial^\mu Z^\nu - \partial^\nu Z^\mu \tag{3.6}$$

and the dual field-strength tensors ($\epsilon^{0123} = +1$)

$$\tilde{F}^{\mu\nu} = \frac{1}{2}\epsilon^{\mu\nu\rho\sigma}F_{\rho\sigma}, \qquad \tilde{Z}^{\mu\nu} = \frac{1}{2}\epsilon^{\mu\nu\rho\sigma}Z_{\rho\sigma}. \tag{3.7}$$

An operator inducing a $\gamma\gamma\gamma$ coupling does not appear in (3.5) since it violates electromagnetic gauge invariance.

Apart from the $\gamma\gamma WW$ coupling which is induced by symmetries in the Lagrangian (3.1), we also include genuine anomalous quartic gauge-boson couplings (AQGC) in our analysis, whose lowest dimension is 6. In [31,32] all genuine dimension-6 AQGC that involve photons and that are allowed by electromagnetic gauge invariance and custodial $\mathrm{SU(2)_c}$ have been classified; more general AQGC have been discussed in [44]. Following [32] we use the effective Lagrangian

$$\begin{aligned}
\mathcal{L}_{\gamma\gamma VV}^\mathrm{AQGC} = -\frac{e^2}{16\Lambda^2}\Big\{&a_0\,F^{\mu\nu}F_{\mu\nu}\overline{\mathbf{W}}_\alpha\overline{\mathbf{W}}^\alpha\\
&+a_\mathrm{c}\,F^{\mu\alpha}F_{\mu\beta}\overline{\mathbf{W}}^\beta\overline{\mathbf{W}}_\alpha\\
&+\tilde{a}_0\,F^{\mu\nu}\tilde{F}_{\mu\nu}\overline{\mathbf{W}}_\alpha\overline{\mathbf{W}}^\alpha\Big\}
\end{aligned} \tag{3.8}$$

with the definition

$$\begin{aligned}
\overline{\mathbf{W}}_\mu &= \left(\overline{W}^1_\mu, \overline{W}^2_\mu, \overline{W}^3_\mu\right) \\
&= \left(\frac{1}{\sqrt{2}}(W^+ + W^-)_\mu, \frac{\mathrm{i}}{\sqrt{2}}(W^+ - W^-)_\mu, \frac{1}{c_\mathrm{w}}Z_\mu\right).
\end{aligned} \tag{3.9}$$

The scale of new physics, Λ, is introduced in (3.8) to render the coupling coefficients $a_0, a_\mathrm{c}, \tilde{a}_0$ dimensionless. The effective Lagrangian $\mathcal{L}_{\gamma\gamma VV}^\mathrm{AQGC}$ contains $\gamma\gamma WW$ and $\gamma\gamma ZZ$ couplings, whose Feynman rules can be found in [32]. The other coupling structures $\mathcal{L}_\mathrm{n}$ and $\tilde{\mathcal{L}}_\mathrm{n}$ considered in [32] induce γZWW couplings that are not relevant for $\gamma\gamma \to 4f$.

3.2 Amplitudes with triple gauge-boson couplings

Before we write down the helicity amplitudes including ATGC explicitly, we discuss the impact of these couplings with respect to the SM cross section. The diagrams containing ATGC and the corresponding quartic couplings in CC diagrams are shown in Fig. 2. We quantify the size of the anomalous contributions in terms of powers of anomalous-coupling factors (generically denoted by a_3) or suppression factors Γ_W/M_W. Considering the SM process $\gamma\gamma \to WW \to 4f$ as the leading contribution, i.e., regarding anomalous-coupling effects as small, we get non-standard contributions to CC and CC/NC cross sections from CC ATGC of the following orders:

(1) $\mathcal{O}(a_3)$: The matrix elements of diagrams (a) and (b) in Fig. 2 involve one power of a_3. Both diagrams are not suppressed by Γ_W/M_W since they are doubly resonant.

[6] Note that our conventions differ from those of [43] by a minus sign in the Z-boson field.

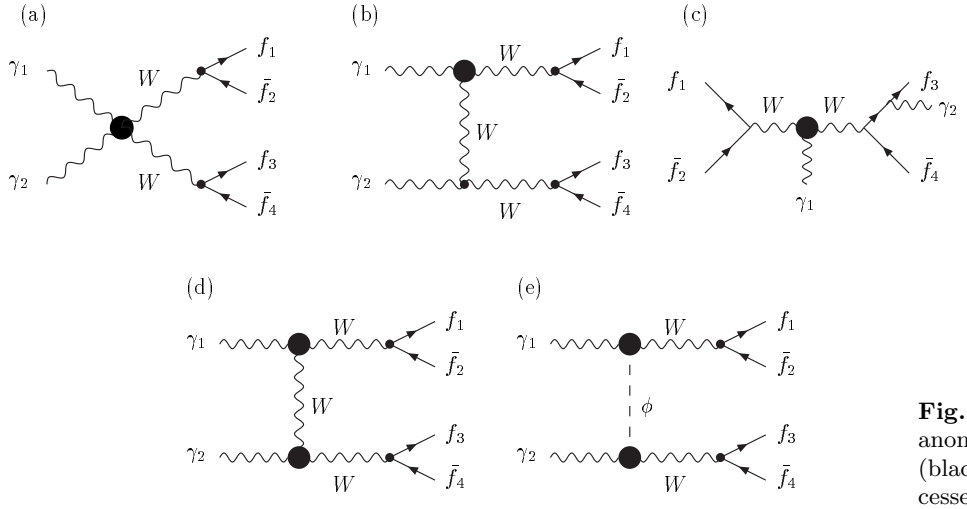

Fig. 2. Representative diagrams with anomalous γWW and $\gamma\gamma WW$ couplings (black blobs) contributing to CC processes $\gamma\gamma \to 4f$

(2) $\mathcal{O}(a_3\Gamma_W/M_W)$: The diagram (c) of Fig. 2 has one power of a_3 and one resonant W boson propagator, i.e., it is only singly resonant. Thus, it is of $\mathcal{O}(a_3\Gamma_W/M_W)$.

(3) $\mathcal{O}(a_3^2)$: The diagrams (d) and (e) of Fig. 2 involve two anomalous couplings a_3 and are doubly resonant. Therefore, they are of $\mathcal{O}(a_3^2)$. Note that the squares of the diagrams (a) and (b), as well as their products with one another, are of the same order as the interference of diagrams (d) and (e) with the SM amplitude.

There are no diagrams containing CC ATGC for NC processes.

Next we consider the impact of NC ATGC, as defined in the effective Lagrangian (3.5). The by far largest SM cross sections of the process class $\gamma\gamma \to 4f$ belong to diagrams with two resonant W bosons in CC and CC/NC reactions. Thus, the largest effect of NC ATGC could be expected from an interference of "anomalous diagrams" with the SM amplitude for CC or CC/NC processes. The only candidate of this kind is a diagram where an off-shell s-channel Z-boson is produced by an anomalous $\gamma\gamma Z$ coupling that subsequently produces a W boson pair. However, the effective $\gamma\gamma Z$ coupling of (3.5) vanishes for two on-shell photons, so that this diagram does not contribute. No other CC diagram exists that includes a NC ATGC.

We now turn to the effects of NC ATGC in NC amplitudes, i.e., in diagrams without W bosons. The corresponding SM amplitudes involve at most a single resonance of the Z-boson, which leads already to a suppression of NC cross sections with respect to CC cross sections by a factor $(\Gamma_Z/M_Z)^2$. This suppression is clearly visible in the numerical results presented in Sect. 6.2.1 below. Diagrams with one NC ATGC also possess at most one resonant Z-boson and, therefore, show a suppression by a factor $a_3(\Gamma_Z/M_Z)^2$ with respect to the CC signal diagrams. This suppression is not changed by interferences with doubly-resonant CC diagrams in CC/NC processes because the Z- and W boson resonances are located at different regions in phase space and do not enhance each other. Diagrams with two NC ATGC can involve two Z-boson resonances resulting in a suppression of $\mathcal{O}(a_3^2\Gamma_Z/M_Z)$, which is also small compared to the CC case owing to the squared ATGC. In summary, we conclude that the sensitivity of the processes $\gamma\gamma \to 4f$ to NC ATGC is much smaller than to CC ATGC. Therefore, we restrict our investigation on ATGC to CC couplings in the following.

As explained above, the diagrams of Fig. 2 induce contributions to the amplitude that are either linear or quadratic in the CC ATGC. We give the explicit contributions to the helicity amplitudes in a way similar to the SM case (2.3),

$$\mathcal{M}^{\sigma_1\sigma_2\sigma_3\sigma_4}_{\lambda_1\lambda_2,\mathrm{CCATGC}}(k_i,p_j,Q_j) = e^4\delta_{\sigma_1,-}\delta_{\sigma_2,+}\delta_{\sigma_3,-}\delta_{\sigma_4,+} \\ g^-_{W\bar{f}_1f_2}g^-_{W\bar{f}_3f_4}\,\delta_3A^{\sigma_1\sigma_3}_{\lambda_1\lambda_2}(k_i,p_j,Q_j), \tag{3.10}$$

with the auxiliary functions $\delta_3A^{\sigma_1\sigma_3}_{\lambda_1\lambda_2}$. The generic amplitude $\mathcal{M}^{\sigma_1\sigma_2\sigma_3\sigma_4}_{\lambda_1\lambda_2,\mathrm{CCATGC}}$ is coherently added to the SM amplitude $\mathcal{M}^{\sigma_1\sigma_2\sigma_3\sigma_4}_{\lambda_1\lambda_2,W}$ of (2.3). The colour summation of the squared amplitudes for the various process types proceeds as described in Sects. 2.3.2 and 2.3.3.

The terms in $\delta_3A^{\sigma_1\sigma_3}_{\lambda_1\lambda_2}$ that are quadratic and linear in ATGC explicitly read

$$\begin{aligned}
\delta_3A^{--}_{++}\Big|_{\mathrm{quad}} &= -P_W(p_1+p_2)P_W(p_3+p_4) \\
&\quad\times P_W(p_1+p_2-k_1)\langle k_1p_1\rangle\langle k_2p_3\rangle \\
&\quad\times\Bigg\{\Delta\kappa_\gamma^2 \\
&\quad\times\left[\langle p_2p_4\rangle^*\langle k_1k_2\rangle + \frac{1}{2M_W^2}\langle p_1p_2\rangle^*\langle p_3p_4\rangle^*\langle k_1p_1\rangle\langle k_2p_3\rangle\right] \\
&\quad+\Delta\kappa_\gamma\frac{\lambda_\gamma}{M_W^2} \\
&\quad\times\left[\langle p_1p_2\rangle^*\langle p_3p_4\rangle^*\left(\langle k_1p_3\rangle\langle k_2p_1\rangle - \langle k_1k_2\rangle\langle p_1p_3\rangle\right)\right. \\
&\quad\quad+\langle k_1k_2\rangle\left(\langle p_3p_4\rangle^*\langle k_1p_2\rangle^*\langle k_1p_3\rangle\right. \\
&\quad\quad\left.\left.-\langle p_1p_2\rangle^*\langle k_2p_4\rangle^*\langle k_2p_1\rangle\right)\right] \\
&\quad+\frac{\lambda_\gamma^2}{M_W^4}\langle p_1p_2\rangle^*\langle p_3p_4\rangle^*\frac{1}{2}(p_1+p_2-k_1)^2
\end{aligned}$$

$$
\begin{aligned}
&\times[\langle k_1p_3\rangle\langle k_2p_1\rangle - \langle k_1k_2\rangle\langle p_1p_3\rangle]\Big\}\\
&+(k_1\leftrightarrow k_2),\\
\delta_3 A^{--}_{+-}\Big|_{\text{quad}} &= -P_W(p_1+p_2)P_W(p_3+p_4)\\
&\times P_W(p_1+p_2-k_1)\langle k_2p_4\rangle^*\langle k_1p_1\rangle\\
&\times\Big\{-\Delta\kappa_\gamma^2\\
&\times\left[\langle k_2p_2\rangle^*\langle k_1p_3\rangle + \frac{1}{2M_W^2}\langle p_1p_2\rangle^*\langle k_2p_4\rangle^*\langle k_1p_1\rangle\langle p_3p_4\rangle\right]\\
&+\Delta\kappa_\gamma\frac{\lambda_\gamma}{M_W^2}\left[-2(p_1+p_2-k_1)^2\langle k_2p_2\rangle^*\langle k_1p_3\rangle\right.\\
&\quad+\langle p_2[K_2-K_1]p_3\rangle\langle k_2[P_1+P_2]k_1\rangle\\
&\quad\left.-\langle p_1p_2\rangle^*\langle k_2p_4\rangle^*\langle p_3p_4\rangle\langle k_1p_1\rangle\right]\\
&+\frac{\lambda_\gamma^2}{M_W^4}\langle p_1p_2\rangle^*\langle p_3p_4\rangle\\
&\times\left[-\frac{1}{2}(p_1+p_2-k_1)^2\langle k_2p_4\rangle^*\langle k_1p_1\rangle\right.\\
&\quad\left.+\langle p_4[K_2-P_3]k_1\rangle\langle k_2[K_1-P_2]p_1\rangle\right]\Big\}\\
&+(\{p_1,Q_1;p_2,Q_2\}\leftrightarrow\{p_3,Q_3;p_4,Q_4\}),\\
\delta_3 A^{--}_{++}\Big|_{\text{lin}} &= 2P_W(p_1+p_2)P_W(p_3+p_4)\langle k_2p_1\rangle\langle k_2p_3\rangle\\
&\times\frac{\langle p_2p_4\rangle^*}{\langle k_1p_2\rangle^*\langle k_1p_4\rangle^*}\\
&\times\left[\Delta\kappa_\gamma\langle p_2p_4\rangle^* - \frac{\lambda_\gamma}{M_W^2}\langle p_3p_4\rangle^*\langle p_1p_2\rangle^*\langle p_1p_3\rangle\right]\\
&+\Big\{2(Q_4-Q_3)P_W(p_3+p_4)P_W(p_3+p_4-k_2)\\
&\times[-Q_1+(Q_1-Q_2)2(k_1p_1)P_W(p_1+p_2)]\\
&\times\frac{\langle k_2p_3\rangle\langle p_2[P_1-K_1]k_2\rangle}{\langle k_1p_1\rangle^*\langle k_1p_2\rangle^*}\\
&\times\left[\Delta\kappa_\gamma\langle p_2p_4\rangle^* + \frac{\lambda_\gamma}{M_W^2}\langle p_3p_4\rangle^*\langle p_2[P_4-K_2]p_3\rangle\right]\\
&\quad+(\{p_1,Q_1;p_2,Q_2\}\leftrightarrow\{p_3,Q_3;p_4,Q_4\})\Big\}\\
&+(k_1\leftrightarrow k_2),\\
\delta_3 A^{--}_{+-}\Big|_{\text{lin}}&\\
&= -2P_W(p_1+p_2)P_W(p_3+p_4)\langle p_1p_3\rangle\frac{\langle k_1p_1\rangle\langle k_1p_3\rangle}{\langle k_2p_1\rangle\langle k_2p_3\rangle}\\
&\times\Big[-\Delta\kappa_\gamma\langle p_2p_4\rangle^*\\
&+\frac{\lambda_\gamma}{M_W^2}\left(\langle p_1p_2\rangle^*\langle k_2p_4\rangle^*\langle k_2p_1\rangle - \langle p_3p_4\rangle^*\langle k_2p_2\rangle^*\langle k_2p_3\rangle\right.\\
&\quad\left.+\langle p_1p_2\rangle^*\langle p_3p_4\rangle^*\langle p_1p_3\rangle\right)\Big]\\
&-\Big\{2(Q_1-Q_2)P_W(p_1+p_2)\\
&\times\Big[[Q_4+(Q_3-Q_4)2(k_2p_4)P_W(p_3+p_4)]\\
&\times P_W(p_1+p_2-k_1)\frac{\langle k_1p_1\rangle\langle k_1p_3\rangle}{\langle k_2p_3\rangle\langle k_2p_4\rangle}\\
&\times\Big(-\Delta\kappa_\gamma\langle p_2[P_4-K_2]p_3\rangle\\
&\quad+\frac{\lambda_\gamma}{M_W^2}\langle p_1p_2\rangle^*\langle p_1p_3\rangle(p_3+p_4-k_2)^2\Big)\Big]\\
&+(\{p_1,Q_1;p_2,Q_2\}\leftrightarrow\{p_3,Q_3;p_4,Q_4\})\Big\} \qquad (3.11)\\
&+(\text{c.c. and }\{p_1,Q_1;p_3,Q_3;k_1\}\leftrightarrow\{p_2,Q_2;p_4,Q_4;k_2\}),
\end{aligned}
$$

where "c.c. and $\{\ldots\}\leftrightarrow\{\ldots\}$" indicates that the complex conjugate of the preceding expression has to be added after some substitutions. The auxiliary functions for the remaining polarizations follow from the relations (2.11) and (2.12).

In order to check our results, we have implemented the ATGC of the effective Lagrangian (3.1) into the program Madgraph [34] and compared our amplitudes with the Madgraph results for various phase-space points. We found perfect numerical agreement.

3.3 Amplitudes with genuine quartic gauge-boson couplings

Figure 3 shows the only diagram with an AQGC (generically denoted by a_4) that contributes to $\gamma\gamma\to 4f$. For CC processes the "anomalous diagram" contributes in $\mathcal{O}(a_4)$ to the cross section, because it is (as the SM contribution) doubly resonant. For NC processes, the diagram involves one power of a_4 and two Z-boson resonances and interferes with the singly-resonant SM amplitude. In this case, the contribution to the corresponding cross section is suppressed by $a_4\Gamma_Z/M_Z$ with respect to CC cross sections, i.e., the suppression factor involves one factor in the anomalous coupling or in Γ_Z/M_Z less than we counted for NC

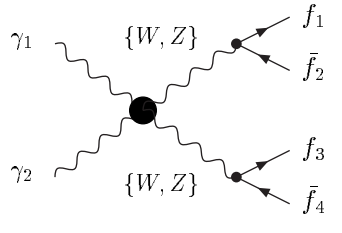

Fig. 3. Diagram with AQGC (black blob) contributing to $\gamma\gamma\to 4f$

ATGC. In the following we take both CC and NC AQGC into account.

The AQGC contributions to the amplitudes read

$$\begin{aligned}&\mathcal{M}^{\sigma_1\sigma_2\sigma_3\sigma_4}_{\lambda_1\lambda_2,\gamma\gamma VV}\\&= \frac{e^4}{8\Lambda^2}\delta_{\sigma_1,-\sigma_2}\delta_{\sigma_3,-\sigma_4}\, g_{\gamma\gamma VV}\, g^{\sigma_1}_{V\bar{f}_1f_2} g^{\sigma_3}_{V\bar{f}_3f_4} \qquad (3.12)\\&\quad\times P_V(p_1+p_2)P_V(p_3+p_4)\delta_4 A^{\sigma_1\sigma_3}_{\lambda_1\lambda_2}(k_1,k_2,p_1,p_2,p_3,p_4),\end{aligned}$$

with

$$g_{\gamma\gamma WW} = 1, \qquad g_{\gamma\gamma ZZ} = \frac{1}{c_{\mathrm{w}}^2} \qquad (3.13)$$

and

$$\begin{aligned}&\delta_4 A^{--}_{++}(k_1,k_2,p_1,p_2,p_3,p_4)\\&= (4a_0 - 4\mathrm{i}\tilde{a}_0 + a_{\mathrm{c}})\langle p_2p_4\rangle^*\langle k_1k_2\rangle^2\langle p_1p_3\rangle,\\&\delta_4 A^{--}_{+-}(k_1,k_2,p_1,p_2,p_3,p_4)\\&= -2a_{\mathrm{c}}\langle k_2p_2\rangle^*\langle k_2p_4\rangle^*\langle k_1p_1\rangle\langle k_1p_3\rangle. \qquad (3.14)\end{aligned}$$

The remaining auxiliary functions $\delta_4 A^{\sigma_1\sigma_3}_{\lambda_1\lambda_2}$ can be obtained via the substitutions

$$\begin{aligned}&\delta_4 A^{\sigma_1,+}_{\lambda_1\lambda_2}(k_1,k_2,p_1,p_2,p_3,p_4)\\&= \delta_4 A^{\sigma_1,-}_{\lambda_1\lambda_2}(k_1,k_2,p_1,p_2,p_4,p_3),\\&\delta_4 A^{+,\sigma_3}_{\lambda_1\lambda_2}(k_1,k_2,p_1,p_2,p_3,p_4)\\&= \delta_4 A^{-,\sigma_3}_{\lambda_1\lambda_2}(k_1,k_2,p_2,p_1,p_3,p_4),\\&\delta_4 A^{\sigma_1\sigma_3}_{\lambda_1\lambda_2}(k_1,k_2,p_1,p_2,p_3,p_4)\\&= \Big(\delta_4 A^{-\sigma_1,-\sigma_3}_{-\lambda_1,-\lambda_2}(k_1,k_2,p_1,p_2,p_3,p_4)\Big)^*. \qquad (3.15)\end{aligned}$$

The generic amplitude $\mathcal{M}^{\sigma_1\sigma_2\sigma_3\sigma_4}_{\lambda_1\lambda_2,\gamma\gamma VV}$ is coherently added to the SM amplitude $\mathcal{M}^{\sigma_1\sigma_2\sigma_3\sigma_4}_{\lambda_1\lambda_2,V}$ of (2.3) for $V = W, Z$, respectively. The colour summation of the squared amplitudes for the various process types proceeds as in the SM case.

Again we have checked the amplitudes against results obtained with Madgraph, as explained at the end of the previous section.

4 Effective $\gamma\gamma H$ coupling and Higgs resonance

In order to incorporate a possible Higgs resonance in $\gamma\gamma \to H \to VV \to 4f$ with $V = W, Z$, as depicted in Fig. 4, we consider an effective coupling of the Higgs boson to two photons. In the SM this coupling is mediated via fermion (mainly top-quark) and W boson loops. We define the effective Lagrangian for the $\gamma\gamma H$ vertex [45] by

$$\mathcal{L}_{\gamma\gamma H} = -\frac{g_{\gamma\gamma H}}{4} F^{\mu\nu}F_{\mu\nu}\frac{H}{v}, \qquad (4.1)$$

where $v = 2M_W s_{\mathrm{w}}/e$ is the vacuum expectation value of the Higgs field H. Up to normalization, $\mathcal{L}_{\gamma\gamma H}$ is the lowest-dimensional, CP-conserving, electromagnetically gauge-invariant operator for two photons and the scalar field H. The corresponding Feynman rule reads

$$\mathrm{i}\Gamma^{\gamma\gamma H}_{\mu\nu}(k_1,k_2,k_H) = \frac{\mathrm{i}g_{\gamma\gamma H}}{v}\left[g_{\mu\nu}(k_1k_2) - k_{1,\nu}k_{2,\mu}\right], \quad (4.2)$$

where k_1, k_2 are the incoming photon momenta. Comparing this Feynman rule to the loop-induced SM vertex with the external fields on shell, which has, e.g., been given in [20, 45], we obtain

$$\begin{aligned}&g_{\gamma\gamma H}\Big|_{\mathrm{SM}} = \frac{\alpha}{\pi} \qquad (4.3)\\&\times\Bigg\{\frac{6M_W^2}{M_H^2} + 1 + \frac{6M_W^2}{M_H^2}(2M_W^2 - M_H^2)C_0(M_H,M_W)\\&\quad -2\sum_f N_f^{\mathrm{c}}Q_f^2\frac{m_f^2}{M_H^2}\left[2 + (4m_f^2 - M_H^2)C_0(M_H,m_f)\right]\Bigg\},\end{aligned}$$

where the colour factor N_f^{c} in the sum over all fermions f is equal to 3 for quarks and 1 for leptons. The scalar 3-point integral C_0 is given by

$$\begin{aligned}C_0(M_H,m) &= \frac{1}{2M_H^2}\ln^2\left(\frac{\beta_m+1}{\beta_m-1}\right),\\ \beta_m &= \sqrt{1 - \frac{4m^2}{M_H^2} + \mathrm{i}\,0.}. \qquad (4.4)\end{aligned}$$

The complete matrix elements for the diagrams with a Higgs resonance (as shown in Fig. 4) can then be written as

$$\begin{aligned}&\mathcal{M}^{\sigma_1\sigma_2\sigma_3\sigma_4}_{\lambda_1\lambda_2,HVV}\\&= -\frac{e^4}{2s_{\mathrm{w}}^2}\,\delta_{\sigma_1,-\sigma_2}\delta_{\sigma_3,-\sigma_4}\, g_{\gamma\gamma H}\, g_{\gamma\gamma VV}\, g^{\sigma_1}_{V\bar{f}_1f_2} g^{\sigma_3}_{V\bar{f}_3f_4}\\&\quad\times P_V(p_1+p_2)P_V(p_3+p_4) \qquad (4.5)\\&\quad\times M_H^2 P_H(k_1+k_2)\,\delta_H A^{\sigma_1\sigma_3}_{\lambda_1\lambda_2}(k_1,k_2,p_1,p_2,p_3,p_4),\end{aligned}$$

with $g_{\gamma\gamma VV}$ defined in (3.13) and

$$\begin{aligned}\delta_H A^{--}_{++}(k_1,k_2,p_1,p_2,p_3,p_4) &= \frac{\langle k_1k_2\rangle}{\langle k_1k_2\rangle^*}\langle p_2p_4\rangle^*\langle p_1p_3\rangle,\\ \delta_H A^{\sigma_1\sigma_3}_{\pm\mp}(k_1,k_2,p_1,p_2,p_3,p_4) &= 0. \qquad (4.6)\end{aligned}$$

The other expressions for $\delta_H A^{\sigma_1\sigma_3}_{\lambda_1\lambda_2}$ follow in the same way as described in (3.15) for $\delta_4 A^{\sigma_1\sigma_3}_{\lambda_1\lambda_2}$. The width in the Higgs-boson propagator P_H is introduced in the same way as in Sect. 2.4 for the gauge bosons.

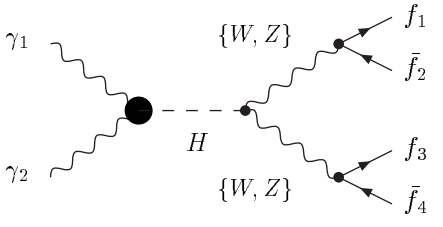

Fig. 4. Diagram with effective $\gamma\gamma H$ coupling (black blob)

5 Monte Carlo integration

The squared matrix element is integrated over the phase space following the strategy described in [16, 41, 46]. We apply the multi-channel Monte Carlo technique [25] where the integrand is flattened by choosing appropriate mappings of the pseudo-random numbers into the momenta of the outgoing particles. This is necessary because the integrand shows a very complex peaking structure in eight ($\gamma\gamma \to 4f$) or eleven ($\gamma\gamma \to 4f\gamma$) dimensions. This complicated structure of the integrand (induced by various diagram types) deteriorates the statistical error of the numerical integration and can lead to numerically unstable results. For each diagram we introduce an own appropriate mapping, so-called "channels", so that more events are generated in regions where the squared matrix element of the diagram is large. The multi-channel approach combines these channels in such a way that the whole integrand is widely smoothed everywhere. For each event a single channel is randomly chosen, and the phase-space configuration is determined according to the mapping of this channel. The probability to choose a given channel, called a priori weight, is optimized according to [26] to minimize the statistical error as much as possible.

The convolution over the photon spectrum is given by

$$\mathrm{d}\sigma = \int_0^1 \mathrm{d}x_1 \int_0^1 \mathrm{d}x_2\, f_\gamma(x_1)\, f_\gamma(x_2)\, \mathrm{d}\sigma_{\gamma\gamma}(x_1P_1, x_2P_2), \tag{5.1}$$

where $\mathrm{d}\sigma_{\gamma\gamma}$ is the differential $\gamma\gamma$ cross section. The function $f_\gamma(x_i)$ denotes the probability density for getting a photon with momentum $k_i = x_iP_i$, and P_i is the electron momentum before Compton backscattering. In order to reduce the statistical error of this integration we use a simple way of stratified sampling. The integration region for x_i of each photon spectrum is divided into a fixed number of bins. We choose bin i with a probability α_i and divide the corresponding weight by α_i. In this way the integration remains formally unchanged if we normalize $\sum_i \alpha_i = 1$. The parameters α_i can be used to improve the convergence of the numerical integration. By choosing the α_i proportional to the cross section of the corresponding bin i, more events are sampled in regions where the photon spectrum is large. Care has to be taken that the α_i do not become too small because this might lead to rare events with very large weights that render the error estimate unreliable. This optimization typically reduces the Monte Carlo integration error by a factor 2–5.

6 Numerical results

6.1 Input parameters

We use the following set of input parameters [47]:

$$\begin{aligned} M_W &= 80.423\,\mathrm{GeV}, & \Gamma_W &= 2.118\,\mathrm{GeV}, \\ M_Z &= 91.1876\,\mathrm{GeV}, & \Gamma_Z &= 2.4952\,\mathrm{GeV}, \\ M_H &= 170\,\mathrm{GeV}, & \Gamma_H &= 0.3834\,\mathrm{GeV}, \\ \alpha(0) &= 1/137.03599976, & \alpha_\mathrm{s} &= 1.1172, \\ G_\mu &= 1.16639 \times 10^{-5}\,\mathrm{GeV}^{-2}, \end{aligned} \tag{6.1}$$

where the Higgs mass is chosen well above the W-pair threshold so that intermediate Higgs bosons decay rapidly into W-pairs; the corresponding decay width Γ_H has been obtained with the program HDECAY [48].

Furthermore, we apply the separation cuts

$$\begin{aligned} &E_\gamma > 10\,\mathrm{GeV}, \quad E_l > 10\,\mathrm{GeV}, \quad E_q > 10\,\mathrm{GeV}, \\ &\theta(\gamma,\mathrm{beam}) > 5^\circ, \quad \theta(l,\gamma) > 5^\circ, \quad \theta(q,\gamma) > 5^\circ, \\ &\theta(l,\mathrm{beam}) > 5^\circ, \quad \theta(l,l') > 5^\circ, \quad \theta(l,q) > 5^\circ, \\ &\theta(q,\mathrm{beam}) > 5^\circ, \quad m(q,q') > 10\,\mathrm{GeV}, \end{aligned} \tag{6.2}$$

where q and l denote quarks and charged leptons, respectively, and $m(q,q')$ is the invariant mass of an outgoing quark pair. The energies E_X and angles $\theta(X,Y)$ are defined in the laboratory frame. Using these cuts all infrared, i.e., soft or collinear, singularities are removed from the phase space.

In order to account for leading universal corrections, we use two different values for the coupling constant $\alpha = e^2/(4\pi)$. Since on-shell photons couple to charged particles with the coupling constant $\alpha(0)$ (effective electromagnetic coupling at zero momentum transfer), we take this coupling for each external photon in the processes $\gamma\gamma \to 4f$ and $\gamma\gamma \to 4f\gamma$. For CC reactions, the remaining couplings correspond to $Wf\bar{f}$ vertices. For these vertices a large part of the electroweak radiative corrections [23] (the running of the electromagnetic coupling and the universal corrections related to the ρ parameter) are absorbed into an effective electromagnetic coupling α_{G_μ} which is derived from the Fermi constant G_μ by

$$\alpha_{G_\mu} = \frac{\sqrt{2} G_\mu M_W^2 s_\mathrm{w}^2}{\pi}. \tag{6.3}$$

Therefore, in the following numerical studies, we replace α^4 by $\alpha(0)^2\alpha_{G_\mu}^2$ for the processes $\gamma\gamma \to 4f$ and α^5 by $\alpha(0)^3\alpha_{G_\mu}^2$ for $\gamma\gamma \to 4f\gamma$.

For the evaluation of the photon spectrum we use the program CompAZ [27] with the polarization of the laser beams -1 (i.e. photon helicity -1)[7] and the polarization of the electron beams $+0.85$. This choice for the relative signs in the polarizations yields a sharper peak at the upper end of the photon spectrum. Results for monochromatic photon beams are always shown for unpolarized photons.

If not stated otherwise, the results are obtained in the fixed-width scheme.

The numerical integration is carried out using 10^7 events. The runtime of our Monte Carlo program on a PC with 2 GHz varies from 30 min to 6 h depending on the considered process.

6.2 Results for integrated cross sections

6.2.1 Survey of cross sections

In order to illustrate the reliability of our Monte Carlo generator we compare our results on cross sections for a

[7] Internally in CompAZ the polarization of the laser light is defined as the negative of the photon helicity.

Table 2. Total cross sections for $\gamma\gamma \to 4f$ at $\sqrt{s} = 500\,\mathrm{GeV}$ for various final states with and without convolution over the photon spectrum

	Present work		Whizard/Madgraph	
$\gamma\gamma \to$	σ_{4f} [fb]	σ_{4f} [fb](conv)	σ_{4f} [fb]	σ_{4f} [fb](conv)
$e^-\bar{\nu}_e\nu_\mu\mu^+$	826.47(21)	190.87(10)	826.39(26)	191.05(16)
$e^-e^+\nu_\mu\bar{\nu}_\mu$	1.75460(62)	0.90525(61)	1.75518(78)	0.9050(11)
$e^-e^+\mu^-\mu^+$	19.400(33)	19.129(61)	19.342(21)	19.188(48)
$e^-e^+e^-e^+$	9.469(17)	9.357(32)	9.453(11)	9.383(25)
$e^-e^+\nu_e\bar{\nu}_e$	828.34(21)	191.72(10)	828.29(26)	191.55(17)
$e^-\bar{\nu}_e u\bar{d}$	2351.11(68)	565.05(33)	2351.79(84)	565.07(51)
$\nu_e e^+ d\bar{u}$	2350.84(68)	558.39(32)	2353.21(84)	558.41(50)
$\nu_e\bar{\nu}_e u\bar{u}$	1.19761(50)	0.61256(50)	1.19684(57)	0.61083(71)
$\nu_e\bar{\nu}_e d\bar{d}$	0.095981(44)	0.049092(45)	0.096011(48)	0.049118(57)
$e^-e^+u\bar{u}$	14.036(21)	10.597(26)	14.016(15)	10.574(21)
$e^-e^+d\bar{d}$	4.7406(29)	2.6614(32)	4.7377(28)	2.6651(38)
$u\bar{d}s\bar{c}$	6659.6(2.1)	1603.8(1.0)	6663.5(2.7)	1605.0(1.5)
$u\bar{u}c\bar{c}$	10.469(14)	6.111(12)	10.4531(88)	6.113(10)
with QCD	1543.6(2.9)	1071.3(2.9)	–	–
$u\bar{u}s\bar{s}$	3.3282(21)	1.6569(18)	3.3310(20)	1.6595(23)
with QCD	412.97(75)	288.79(72)	–	–
$d\bar{d}s\bar{s}$	0.49807(29)	0.23232(24)	0.49804(30)	0.23252(32)
with QCD	96.34(18)	66.80(18)	–	–
$u\bar{u}u\bar{u}$	5.1846(69)	3.0298(57)	5.1900(45)	3.0419(53)
with QCD	772.6(1.5)	538.9(1.4)	–	–
$d\bar{d}d\bar{d}$	0.24683(15)	0.11581(12)	0.24665(17)	0.11579(17)
with QCD	48.252(96)	33.685(88)	–	–
$u\bar{u}d\bar{d}$	6663.5(2.3)	1606.1(1.1)	6664.8(2.8)	1604.6(1.6)
with QCD	7075.8(3.7)	1896.4(2.9)	–	–

representative set of the processes $\gamma\gamma \to 4f$ and $\gamma\gamma \to 4f\gamma$ with the results obtained with the Monte Carlo program Whizard (version 1.28) [33] which uses the matrix-element generator Madgraph [34][8]. In Tables 2 and 3 we list the results for the 17 different final states defined in Table 1. The numbers in parentheses correspond to the Monte Carlo error. For the final states that can be produced via intermediate gluons we compute the cross section both with and without gluon-exchange contributions. Since the version of Madgraph implemented in Whizard is not able to deal with interferences of electroweak and QCD diagrams, we give only the pure electroweak Whizard/Madgraph results for these processes. Furthermore, we list the corresponding cross sections with and without convolution over the photon beam spectrum. For this study, we have implemented the program CompAZ into Whizard.

As explained in Sect. 2.2, the cross sections for the CP-equivalent final states $e^-\bar{\nu}_e u\bar{d}(\gamma)$ and $\nu_e e^+ d\bar{u}(\gamma)$ are not identical if the convolution over the photon beam spectrum is carried out. Therefore, we give results for both final states. In all other cases, the cross sections for a given final state and for the CP-conjugated one coincide.

[8] For a tuned comparison we rescaled the Whizard/Madgraph results by a factor $\alpha(0)^2\alpha_{G_\mu}^2/\alpha^4$ for $\gamma\gamma \to 4f$ and $\alpha(0)^3\alpha_{G_\mu}^2/\alpha^5$ for $\gamma\gamma \to 4f\gamma$.

CC and CC/NC processes possess the largest cross sections because of the dominance of W-pair production. The convolution over the photon spectrum reduces these cross sections significantly since low-energy photons cannot produce on-shell W-pairs. NC processes are affected less, and in some cases, such as $\gamma\gamma \to e^+e^-\mu^+\mu^-$, the cross section is only slightly reduced. Owing to the colour factors of the quarks, hadronic and semi-leptonic cross sections differ by roughly a factor 3, hadronic and leptonic cross sections by roughly a factor $3^2 = 9$. For CC processes $\gamma\gamma \to 4f$ we obtain a rough estimate of the cross sections by multiplying the cross section of $\gamma\gamma \to WW$ with the branching ratios of the W bosons into leptons or quarks depending on the final state. Note that this estimate, which is only good within 10−20%, does not take into account contributions from background diagrams, width effects, and cuts on final-state fermions. The difference of cross sections for CC processes and the corresponding processes of mixed type reflects the size of the background contributions induced by NC diagrams.

The results of Whizard, which are also generated with 10^7 events, and of our program typically agree within 1–2 standard errors. The size of the statistical errors obtained with Whizard and our program is comparable. The runtime of Whizard is usually somewhat bigger than the one of our program. Depending on the process class, the speed of our

Table 3. Total cross sections for $\gamma\gamma \to 4f\gamma$ at $\sqrt{s} = 500\,\mathrm{GeV}$ for various final states with and without convolution over the photon spectrum

	Present work		Whizard/Madgraph	
$\gamma\gamma \to$	$\sigma_{4f\gamma}$ [fb]	$\sigma_{4f\gamma}$ [fb](conv)	$\sigma_{4f\gamma}$ [fb]	$\sigma_{4f\gamma}$ [fb](conv)
$e^-\bar{\nu}_e\nu_\mu\mu^+\gamma$	39.234(44)	6.188(11)	39.218(29)	6.2040(87)
$e^-e^+\nu_\mu\bar{\nu}_\mu\gamma$	0.10157(10)	0.028612(40)	0.101556(88)	0.028548(52)
$e^-e^+\mu^-\mu^+\gamma$	1.0567(35)	0.5083(28)	1.0547(20)	0.5091(29)
$e^-e^+e^-e^+\gamma$	0.5085(18)	0.2433(13)	0.5091(10)	0.2461(12)
$e^-e^+\nu_e\bar{\nu}_e\gamma$	39.301(46)	6.213(11)	39.332(30)	6.2069(89)
$e^-\bar{\nu}_e u\bar{d}\gamma$	96.61(13)	14.216(27)	96.575(75)	14.159(21)
$\nu_e e^+ d\bar{u}\gamma$	96.60(13)	15.459(30)	96.520(76)	15.429(22)
$\nu_e\bar{\nu}_e u\bar{u}\gamma$	0.030818(35)	0.008640(14)	0.030756(28)	0.008609(16)
$\nu_e\bar{\nu}_e d\bar{d}\gamma$	0.00061753(75)	0.00017313(31)	0.00061731(56)	0.00017358(34)
$e^-e^+u\bar{u}\gamma$	0.6446(17)	0.25463(99)	0.6477(10)	0.2579(10)
$e^-e^+d\bar{d}\gamma$	0.26653(36)	0.08137(17)	0.26689(28)	0.08166(21)
$u\bar{d}s\bar{c}\gamma$	229.86(36)	32.621(81)	229.52(19)	32.531(49)
$u\bar{u}c\bar{c}\gamma$	0.30556(69)	0.10718(34)	0.30563(47)	0.10836(43)
with QCD	34.73(14)	13.801(77)	–	–
$u\bar{u}s\bar{s}\gamma$	0.08791(13)	0.026278(59)	0.087935(98)	0.026271(65)
with QCD	6.362(23)	2.493(13)	–	–
$d\bar{d}s\bar{s}\gamma$	0.0046253(71)	0.0014842(37)	0.0046191(52)	0.0014832(36)
with QCD	0.5427(22)	0.2165(11)	–	–
$u\bar{u}u\bar{u}\gamma$	0.15081(33)	0.05301(16)	0.15082(21)	0.05332(16)
with QCD	17.377(71)	6.964(35)	–	–
$d\bar{d}d\bar{d}\gamma$	0.0022893(37)	0.0007421(21)	0.0022878(25)	0.0007398(18)
with QCD	0.2716(11)	0.10863(53)	–	–
$u\bar{u}d\bar{d}\gamma$	229.86(40)	32.85(15)	229.65(19)	32.518(51)
with QCD	236.31(42)	35.14(11)	–	–

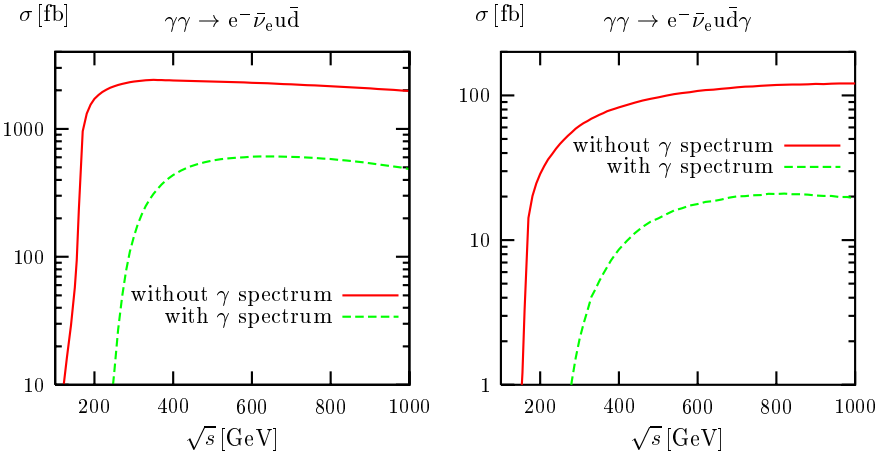

Fig. 5. Integrated cross sections of the processes $\gamma\gamma \to e^-\bar{\nu}_e u\bar{d}(\gamma)$ with and without convolution over the photon spectrum as a function of the CM energy $\sqrt{s}$

program is 1−7 times higher, where the largest difference occurs for NC processes.

6.2.2 Energy dependence of integrated cross sections

In Fig. 5 we show the cross sections for the processes $\gamma\gamma \to e^-\bar{\nu}_e u\bar{d}(\gamma)$ as a function of the centre-of-mass (CM) energy $\sqrt{s}$ with and without convolution over the photon spectrum. Here and in the following, with convolution over the photon spectrum $\sqrt{s}$ stands for the CM energy $\sqrt{s_{ee}}$ of the incoming electron beams; without convolution it is the CM energy $\sqrt{s_{\gamma\gamma}}$ of the incoming photons. In the case without photon spectrum, the rise of the cross section is clearly visible at the W-pair threshold, $\sqrt{s_{\gamma\gamma}} \gtrsim 160\,\mathrm{GeV}$. For $\gamma\gamma \to e^-\bar{\nu}_e u\bar{d}$ the cross section increases roughly proportional to $\beta = \sqrt{1 - 4M_W^2/s_{\gamma\gamma}}$ above the threshold, as expected from the two-particle phase space of the W-pairs. For $\gamma\gamma \to e^-\bar{\nu}_e u\bar{d}\gamma$ the rise of the cross section is not

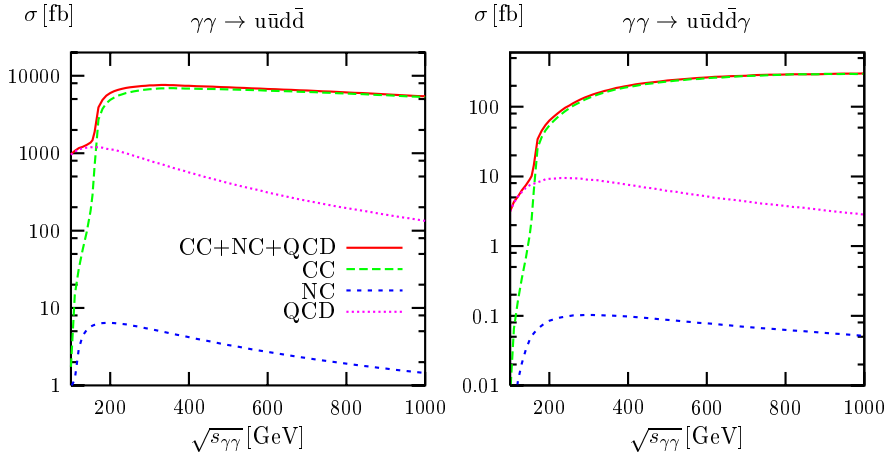

Fig. 6. Different contributions to the integrated cross sections for the processes $\gamma\gamma \to u\bar{u}d\bar{d}(\gamma)$ as a function of the CM energy without photon spectrum

as steep because of the higher-dimensional $WW\gamma$ phase space. The convolution over the photon spectrum reduces the available energy for W-pair production and shifts the onset of the cross section to higher CM energies.

The cross sections for $\gamma\gamma \to 4f$ as well as $\gamma\gamma \to 4f\gamma$ decrease at high energies, even though the total cross section of the $\gamma\gamma \to WW$ process approaches a constant in the high-energy limit if no cuts are imposed, i.e., if the W bosons are allowed to go in the beam directions. At high energies, however, forward and backward scattering of W bosons is restricted due to the cuts applied to the outgoing fermions, because the decay fermions mainly follow the direction of the decaying W boson.

6.2.3 Contributions from CC, NC, and gluon-exchange diagrams

In Fig. 6 we show the impact of CC, NC, and gluon-exchange diagrams on the CC/NC processes $\gamma\gamma \to u\bar{u}d\bar{d}$ and $\gamma\gamma \to u\bar{u}d\bar{d}\gamma$. We do not include the photon spectrum in this analysis. Above the W-pair threshold, $\sqrt{s_{\gamma\gamma}} > 160\,\text{GeV}$, the CC diagrams are clearly dominating, while the contributions from gluon-exchange diagrams are one or two orders of magnitude smaller. The impact of the gluon-exchange diagrams strongly depends on the choice of the invariant-mass cut between two quarks, and gluon-exchange diagrams are more important if the invariant-mass cut is small. The contributions from pure NC diagrams are totally negligible as long as W-pair production is possible.

6.2.4 W-pair signal diagrams and double-pole approximation

In Fig. 7 the cross sections of the W-pair signal diagrams and the DPA for $\gamma\gamma \to WW \to 4f$ (see Sect. 2.5 for definitions) are compared with the complete lowest-order cross section for several processes. The plots on the LHS show the cross sections for various final states calculated from the full set of (electroweak) diagrams, from the signal diagrams only, and in DPA separately for hadronic, semi-leptonic, and leptonic final states, while the plots on the RHS show the relative deviation from the corresponding DPA. We do not include the convolution over the photon spectrum and gluon-exchange diagrams in this analysis so that effects of the approximation are clearly visible. For energies not too close to the W-pair threshold, the DPA agrees with the full lowest-order cross section within 1–3%, which is of the expected order of Γ_W/M_W. Near threshold, i.e. for $\sqrt{s_{\gamma\gamma}} - 2M_W = \mathcal{O}(\Gamma_W)$, the reliability of the DPA breaks down, since background diagrams become more and more important and small scales γ, such as $\sqrt{s_{\gamma\gamma} - 4M_W^2}$, can increase the naive error estimate from Γ_W/M_W to Γ_W/γ. The cross sections of the W-pair signal diagrams, however, shows large deviations from the full $\gamma\gamma \to 4f$ cross sections for the whole energy range, in particular, at high energies. As explained in Sect. 2.5, the W-pair signal diagrams are not gauge invariant, and thus the reliability and usefulness of the resulting predictions should be investigated carefully. The results of Fig. 7 clearly show that a naive signal definition is a bad concept for $\gamma\gamma \to WW \to 4f$, since deviations from the full process $\gamma\gamma \to 4f$ even reach 5–10% in the TeV range. This is in contrast to the situation at e^+e^- colliders where the naive W-pair signal (defined in 't Hooft–Feynman gauge) was a reasonable approximation (see, e.g., [35]).

The failure of the naive W-pair signal definition for $\gamma\gamma$ collisions was also pointed out in [6, 7] before. In [7] an "improved narrow-width approximation" was presented which provides another variant for a gauge-invariant W-pair signal definition. It is based on the factorization of production and decay matrix elements, while retaining W-spin correlations.

6.2.5 Comparison of schemes for introducing finite gauge-boson widths

In this section we compare the different implementations of gauge-boson widths described in Sect. 2.4 numerically. As explained in Sect. 2.4, the complex-mass scheme is the only scheme that yields gauge-invariant results in general, but for the process classes $\gamma\gamma \to 4f(\gamma)$ the fixed-width approach (in the non-linear gauge) also yields amplitudes that respect Ward identities and gauge cancellations. Table 4 lists the cross sections for the processes $\gamma\gamma \to e^-\bar{\nu}_e\nu_\mu\mu^+$

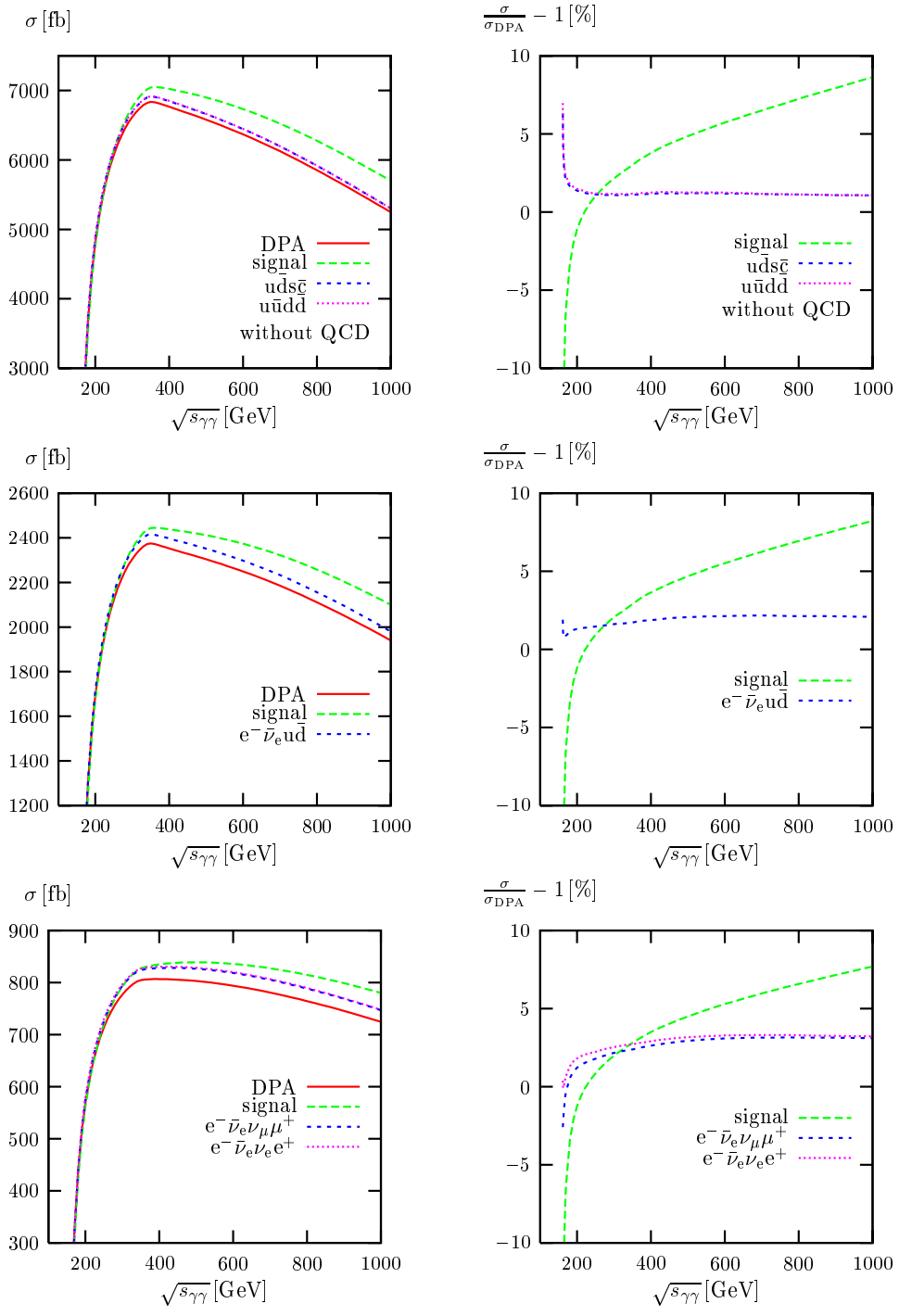

Fig. 7. Cross sections of various processes including all diagrams, only W-pair signal diagrams, and in DPA as a function of the CM energy (LHS), and the corresponding relative deviations from the DPA (RHS); photon spectrum and gluon-exchange diagrams are not included

and $\gamma\gamma \to e^-\bar{\nu}_e\nu_\mu\mu^+\gamma$ obtained with the fixed W-width, the step-width, the running-width, and with the complex-mass scheme. The results of all four schemes for the process $\gamma\gamma \to e^-\bar{\nu}_e\nu_\mu\mu^+$ agree within the expected accuracy of $\mathcal{O}(\Gamma_W/M_W)$ up to energies in the TeV range. However, for $\gamma\gamma \to e^-\bar{\nu}_e\nu_\mu\mu^+\gamma$ the running-width scheme yields totally wrong results for several TeV, while the other schemes are still in good agreement. Although the gauge-invariance-breaking effects in the running-width scheme are formally of $\mathcal{O}(\Gamma_W/M_W)$, they are enhanced by spoiling gauge cancellations, thereby ruining the reliability of the prediction completely.

For the semi-leptonic $\gamma\gamma \to 4f$ process it was already observed in [7] that the cross section does not vary significantly if the fixed-width, the running-width, or a so-called "fudge-factor" scheme is used for introducing finite widths.

Table 4. Cross sections for the processes $\gamma\gamma \to e^-\bar{\nu}_e\nu_\mu\mu^+$ and $\gamma\gamma \to e^-\bar{\nu}_e\nu_\mu\mu^+\gamma$ for various CM energies and various width schemes without convolution over the photon spectrum

$\sqrt{s_{\gamma\gamma}}$ [GeV]	500	800	1000	2000	10000
			$\sigma(\gamma\gamma \to e^-\bar{\nu}_e\nu_\mu\mu^+)$		
fixed width	826.40(21)	788.35(21)	746.94(21)	500.70(20)	31.745(68)
step width	827.45(22)	789.34(21)	748.17(23)	501.41(21)	31.746(68)
running width	827.43(23)	789.29(21)	748.11(23)	501.32(21)	31.715(68)
complex mass	826.23(21)	788.18(21)	746.78(21)	500.59(20)	31.738(68)
			$\sigma(\gamma\gamma \to e^-\bar{\nu}_e\nu_\mu\mu^+\gamma)$		
fixed width	39.230(45)	47.740(73)	49.781(91)	43.98(18)	4.32(23)
step width	39.253(45)	47.781(73)	49.881(96)	44.01(18)	4.31(24)
running width	39.251(49)	47.781(74)	49.898(95)	44.48(22)	10.83(28)
complex mass	39.221(45)	47.730(73)	49.770(91)	43.97(18)	4.31(23)

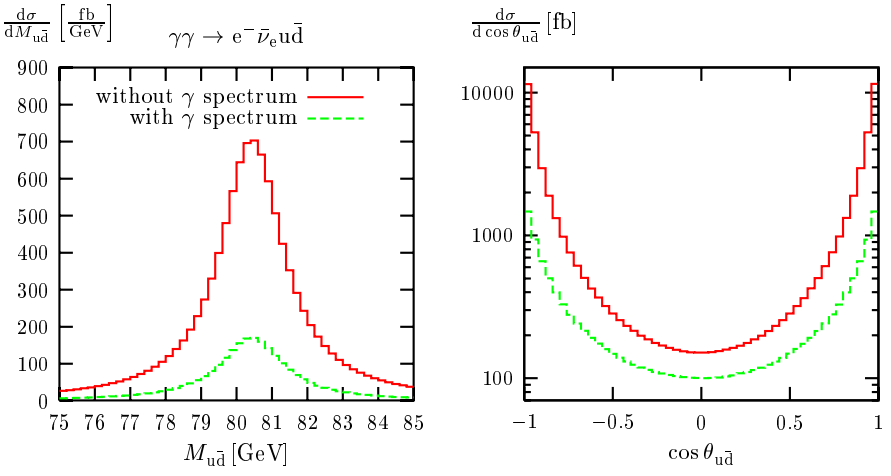

Fig. 8. Invariant-mass distribution of the W^+-boson reconstructed from the $u\bar{d}$ quark pair (LHS) as well as its production-angle distribution (RHS) in the reaction $\gamma\gamma \to e^-\bar{\nu}_e u\bar{d}$ at $\sqrt{s} = 500\,\text{GeV}$ with and without convolution over the photon spectrum

6.3 Distributions

6.3.1 Distributions for reconstructed W bosons

In Fig. 8 we show the invariant-mass and angular distributions of the intermediate W^+-boson for the process $\gamma\gamma \to e^-\bar{\nu}_e u\bar{d}$ at $\sqrt{s} = 500\,\text{GeV}$. The momentum of the W^+-boson is reconstructed from the outgoing quark pair in the decay $W^+ \to u\bar{d}$. Figure 8 also illustrates the effect of the convolution over the photon spectrum.

The resonance in the invariant-mass distribution (LHS of Fig. 8) has the typical Breit–Wigner shape and can be used to determine the W boson mass and width at a $\gamma\gamma$ collider. Moreover, owing to its large cross section, the W-reconstruction in this reaction seems to be a promising possibility for detector calibration at a $\gamma\gamma$ collider. Similarly to the integrated cross sections discussed in the previous sections, the convolution qualitatively rescales the distribution by roughly a factor 4.

The RHS of Fig. 8 shows the distribution in the angle $\theta_{u\bar{d}}$ between the W^+-boson and the beam axis. Since the incoming $\gamma\gamma$ state is symmetric with respect to interchange of the two photons, the angular distribution is symmetric in the production angle $\theta_{u\bar{d}}$. W bosons are predominantly produced in forward or backward direction owing to diagrams with t- and u-channel exchange of W bosons. For the process $\gamma\gamma \to WW$ with on-shell W bosons, the forward and backward peaks are integrable and lead to a constant cross section in the high-energy limit. As already pointed out in Sect. 6.2.2, the angular cuts (6.2) restrict the available phase space of the intermediate W bosons and lead to a reduction of the forward and backward peaks for sufficiently high energies. Note that the reduction induced by the convolution over the photon spectrum is not uniform, but tends to flatten the shape of the angular distribution slightly. This is mainly due to the reduced CM energy in the photon spectrum, leading to a less pronounced peaking behaviour in the forward and backward directions.

6.3.2 Energy and production-angle distributions of fermions

In Fig. 9 we show the energy and angular distributions of the outgoing fermions e^-, u, and $\bar{d}$ in the reaction $\gamma\gamma \to e^-\bar{\nu}_e u\bar{d}$ at $\sqrt{s} = 500\,\text{GeV}$ with and without convolution over the photon spectrum.

For monochromatic, unpolarized incoming γ beams (i.e. without convolution over the photon spectrum), the energy distributions (LHS of Fig. 9) of the fermions e^-, u, and $\bar{d}$ almost coincide and are maximal at their largest and smallest kinematical limits. These regions are dominated by the

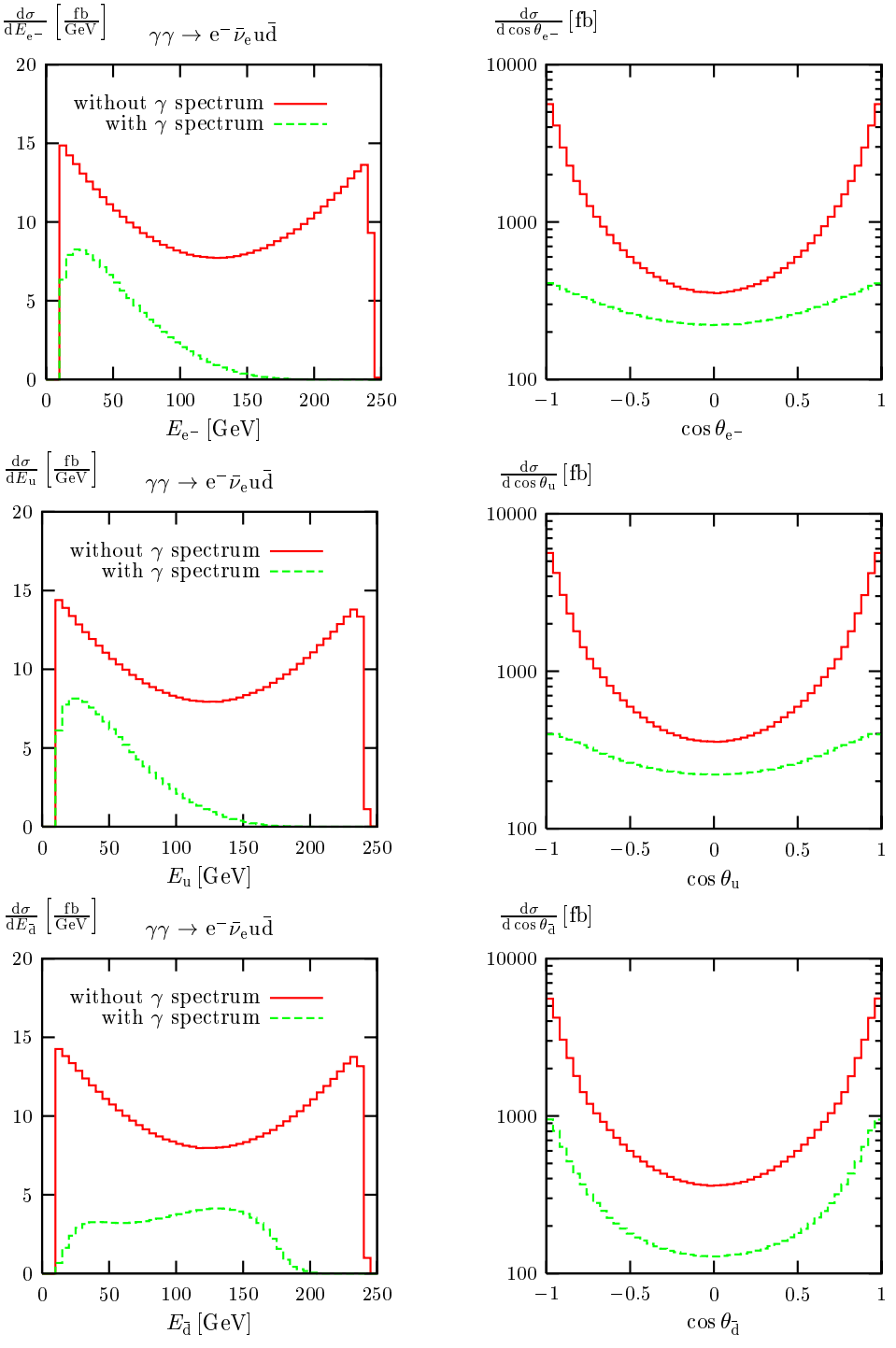

Fig. 9. Energy (LHS) and production-angle (RHS) distributions of the outgoing fermions e^-, u, and $\bar{d}$ in the process $\gamma\gamma \to e^-\bar{\nu}_e u\bar{d}$ at $\sqrt{s} = 500\,\text{GeV}$ with and without convolution over the photon spectrum

situations where the respective W boson emits the considered fermion parallel or anti-parallel to its direction of flight. The convolution over the photon spectrum changes the shapes of the energy distributions considerably. Since the photon spectrum falls off rapidly for energies above 80% of the incoming electron energy, energies of the final-state fermions larger than 200 GeV become practically impossible. For fermion energies below 200 GeV the shapes of the distributions of the outgoing fermions e^- and u look rather different from the one for the anti-fermion $\bar{d}$. This effect is due to the effective γ beam polarization in the photon spectrum; for unpolarized γ beams the energy distributions would look almost identical. In detail, the effective polarization of the $\gamma\gamma$ system is mainly $(\lambda_1\lambda_2) = (++)$, leading predominantly to W^+W^- production with effective helicities $(++)$ (see, e.g., [7,21]). Owing to helicity conservation, however, W bosons with helicity $+1$ cannot decay into fermion–anti-fermion pairs with a fermion (which must have helicity $-\frac{1}{2}$) parallel to the flight direction of the W boson. Thus, much more anti-fermions (which

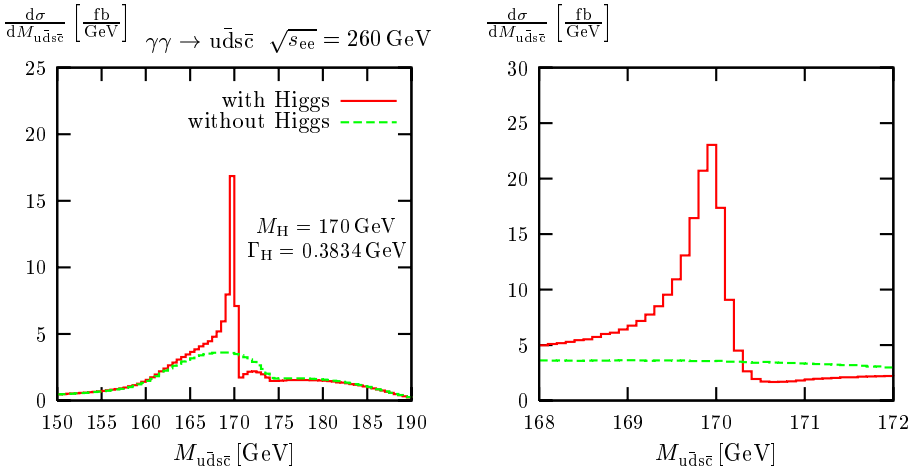

Fig. 10. Invariant-mass distribution of the four-quark final state for the process $\gamma\gamma \to u\bar{d}s\bar{c}$ at $\sqrt{s_{ee}} = 260\,\mathrm{GeV}$ including convolution over the photon spectrum

have helicity $+\frac{1}{2}$) than fermions follow the directions of the decaying W bosons, which qualitatively explains the reduction (enhancement) of the fermion (anti-fermion) energy distributions at the upper kinematical energy limit. The above arguments are nicely illustrated in [7], where the fermion energy distributions are shown for fully polarized, monochromatic photon beams.

The RHS of Fig. 9 shows the distributions in the angles θ_f of the (anti-)fermions $f = e^-, u, \bar{d}$ to the beam axis. Because of the symmetry of the incoming $\gamma\gamma$ state with respect to interchange of the two photons, the angular distribution is symmetric in θ_f. The forward and backward peaks originate from two sources. The by far largest contribution to the differential cross section comes from signal diagrams and thus from configurations where the W bosons as well as the decay fermions are nearly parallel to the beam. The second source, which is widely suppressed by the applied cuts, is related to collinear singularities of background diagrams where an incoming photon splits into an fermion–anti-fermion pair $f\bar{f}$, with the fermion or anti-fermion directly going into the final state. If the phase space of the outgoing (anti-)fermion is not restricted by cuts, such collinear or mass singularities lead to logarithms of the form $\ln(s/m_f^2)$, where m_f is the fermion mass. Since our calculation is done for massless fermions, the collinear singularities must be excluded by phase-space cuts and the fermion mass in $\ln(s/m_f^2)$ is replaced by the corresponding cut parameter.

The photon spectrum reduces the differential cross section over the whole range and again flattens the angular distributions, especially in the cases of outgoing fermions. The significant difference between the outgoing fermions and anti-fermions is again due to the effective γ polarization in the photon spectrum. As explained above, more anti-fermions than fermions follow the flight directions of the W bosons, which are mainly produced in the forward and backward directions. This is the reason why the θ_{e^-} and θ_u distributions are flattened, while the peaking behaviour in the $\theta_{\bar{d}}$ distribution is more pronounced after the convolution over the photon spectrum.

6.3.3 Higgs-boson resonance

In Fig. 10 we show the invariant-mass distribution of the Higgs boson for the process $\gamma\gamma \to H \to WW \to u\bar{d}s\bar{c}$ for a Higgs mass of $M_H = 170\,\mathrm{GeV}$. The CM energy of the electron beams is chosen to be $\sqrt{s_{ee}} = 260\,\mathrm{GeV}$ which maximizes the $\gamma\gamma$ luminosity in the region $\sqrt{s_{\gamma\gamma}} \sim M_H$. The invariant mass $M_{u\bar{d}s\bar{c}}$ of the Higgs boson is reconstructed from its decay products which are the four outgoing quarks. This means that $M_{u\bar{d}s\bar{c}}$ is equal to the photonic CM energy, $M_{u\bar{d}s\bar{c}} = \sqrt{s_{\gamma\gamma}}$. Thus, the shape of the distribution depends on the form of the photon spectrum very strongly. The effective $\gamma\gamma H$ coupling is set to the SM value (4.3). For comparison the situation without Higgs resonance is also included in Fig. 10, illustrating the significance of the Higgs signal. The different peak heights in the two plots simply result from different bin sizes.

6.4 Anomalous couplings

In this section we study the impact of possible anomalous gauge-boson couplings on CC cross sections of the process class $\gamma\gamma \to 4f$. In order to estimate the full sensitivity of a future $\gamma\gamma$ collider, such as the $\gamma\gamma$ option at TESLA, on anomalous couplings, in addition differential distributions and realistic event selections should be taken into account. Such a study goes beyond the scope of this paper, but our Monte Carlo generator can serve as a tool in this task.

We consider only semi-leptonic final states, since these have the cleanest experimental signal. The cross section for semi-leptonic final states is obtained from the sum over all reactions $\gamma\gamma \to l^-\bar{\nu}_l q\bar{q}'$, with $q = u, c$ and $l = e, \mu, \tau$, and their corresponding charge-conjugated processes $\gamma\gamma \to \nu_l l^+ q'\bar{q}$. The results are shown in Fig. 11 for ATGC and in Fig. 12 for AQGC. In the left plot of Fig. 11 and the upper plot of Fig. 12 we show the cross section as a function of the anomalous-coupling constant normalized to the SM cross section. As can be seen in the insert of Fig. 11, the minimum in the $\Delta\kappa_\gamma$ curve is shifted to negative values which is caused by contributions to the cross section that are linear in $\Delta\kappa_\gamma$. These contributions result from the interference

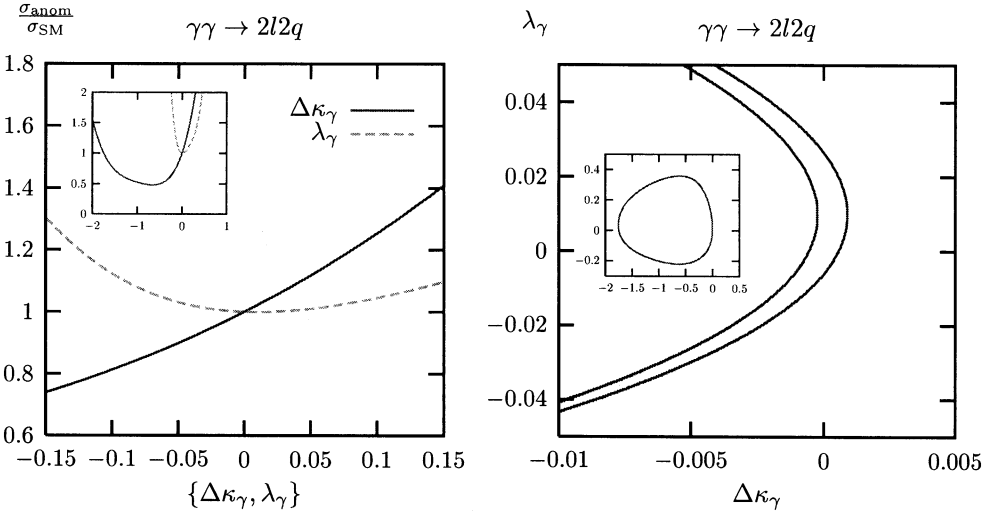

Fig. 11. Combined cross section for semi-leptonic final states as a function of the ATGC $\Delta\kappa_\gamma$ and λ_γ (LHS) and 1σ contours (RHS) in the $(\Delta\kappa_\gamma, \lambda_\gamma)$ plane at $\sqrt{s_{ee}} = 500\,\mathrm{GeV}$ including the convolution over the photon spectrum

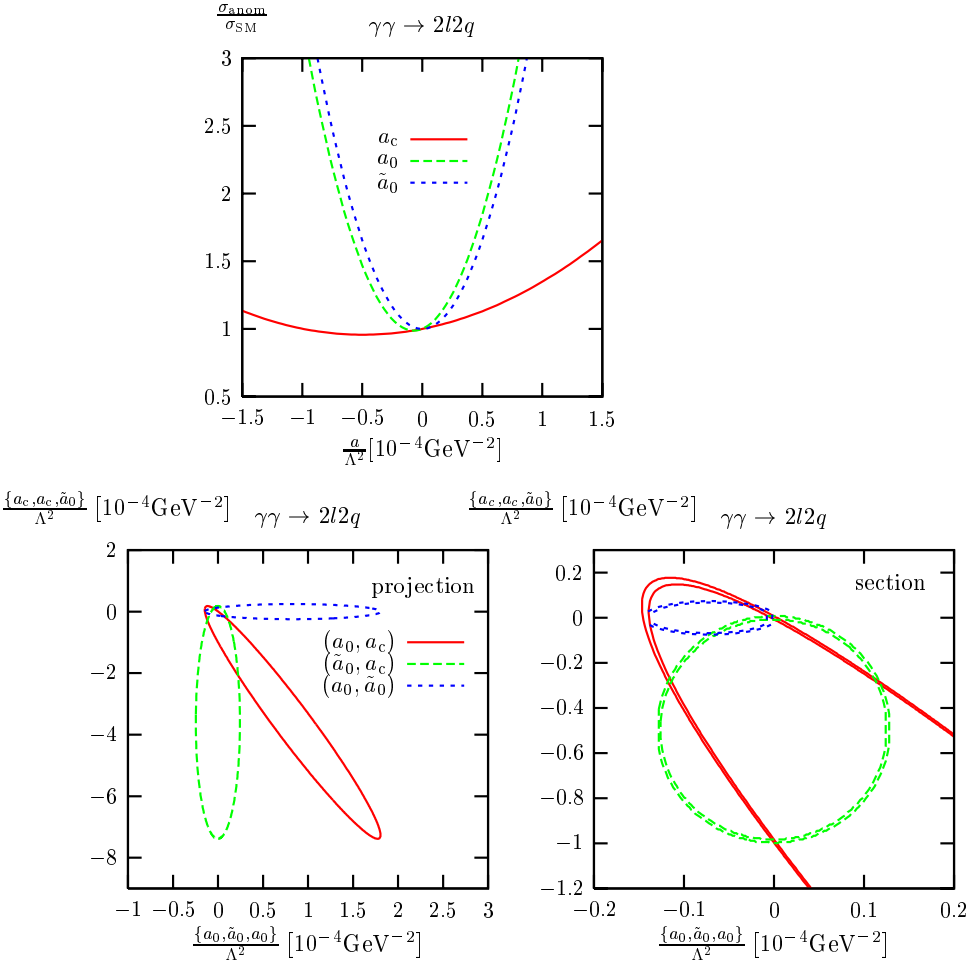

Fig. 12. Combined cross section for semi-leptonic final states as a function of the AQGC a_0, $a_{\rm c}$, and $\tilde{a}_0$ (upper plot) and 1σ contours (LHS projection, RHS section) in the coordinate planes at $\sqrt{s_{ee}} = 500\,\mathrm{GeV}$ including the convolution over the photon spectrum

between matrix elements linear in the ATGC $\Delta\kappa_\gamma$ with the SM amplitude. On the other hand, the interferences for the ATGC λ_γ are small. In the case of AQGC, such interferences are relatively large for $a_{\rm c}$.

In order to examine the sensitivity of a linear collider to anomalous couplings, we consider a $\gamma\gamma$ collider with an integrated luminosity of $\mathcal{L} = 100\,\mathrm{fb}^{-1}$ and a CM energy of $\sqrt{s_{ee}} = 500\,\mathrm{GeV}$ [1]. We define

$$\chi^2 \equiv \frac{(N(a_i) - N)^2}{N} \quad \text{with} \quad N = \sigma_{\rm SM}\mathcal{L}, \quad N(a_i) = \sigma(a_i)\mathcal{L}, \quad (6.4)$$

where N is the expected number of events in the SM and $N(a_i)$ the number of events in the SM extended by the non-standard couplings. In Figs. 11 and 12 the 1σ contours corresponding to $\chi^2 = 1$ are shown. Note that the

1σ contour can result from $N(a_i) > N$ and $N(a_i) < N$. While $\chi^2 = 1$ with $N(a_i) > N$ is always possible for sufficiently large anomalous couplings, $\chi^2 = 1$ with $N(a_i) < N$ requires large interference effects of matrix elements with anomalous couplings. In our case, both branches of the 1σ contours are realized. In Fig. 11 the plot on the RHS shows the 1σ contours in the $(\Delta\kappa_\gamma, \lambda_\gamma)$ plane. Since the cross section is a polynomial up to fourth power in the ATGC, the contours are not of elliptic form. The allowed region lies between the two contours that are rather close to each other so that they cannot be distinguished in the insert which shows the contours on a larger scale. Note that in the limit of large luminosity the contour in the insert of the RHS of Fig. 11 does not shrink to a point, but reduces to a line in the $(\Delta\kappa_\gamma, \lambda_\gamma)$ plane on which $\sigma_{\mathrm{anom}} = \sigma_{\mathrm{SM}}$. In order to resolve this correlation between $\Delta\kappa_\gamma$ and λ_γ, anomalous effects on distributions should be considered, or other constraints from the e^+e^- or $e^-\gamma$ modes should be included.

In case of AQGC the cross section is at most quadratic in the AQGC, and the $\chi^2 = 1$ surface consists of two ellipsoids in the $(a_0, a_c, \tilde{a}_0)$ space. The existence of two branches is again due to large interferences of anomalous contributions. In the lower left plot of Fig. 12 we show the projections of the outer ellipsoid into the coordinate planes of two AQGC (where the third AQGC is zero). In the lower right plot the sections of both ellipsoids with these planes are given. Since the centre of the ellipsoids is shifted in the a_c and a_0 directions, the terms in $\sigma(a_i)$ linear in these couplings are significant; they result from interferences of the diagram with the AQGC with the SM amplitude. Interferences that are proportional to $\tilde{a}_0$ turn out to be small. From (3.14) it is obvious that there are no $a_0\tilde{a}_0$ and $a_c\tilde{a}_0$ terms in $\sigma(a_i)$. Consequently, the projection into and the section with the (a_0, a_c) plane coincide. On the other hand, the two other projections and sections differ, signalling that the $a_c a_0$ term in $\sigma(a_i)$ is significant.

The allowed 1σ region ($\chi^2 < 1$) in the $(a_0, a_c, \tilde{a}_0)$ space is the shell at the boundary of the shown ellipsoid. Similar to the observation made above for the ATGC, the size of the ellipsoid does not shrink for larger luminosity, only the thickness of the shell will decrease. This means that the size of the projections shown in the lower left plot of Fig. 12 will not reduce for larger luminosity. Thus, using only information on an integrated cross section (for a fixed energy) could not improve the bounds on AQGC with respect to the ones resulting from $e^+e^- \to WW\gamma \to 4f\gamma$ [32]. However, the thinness of the shell of the ellipsoid, as illustrated in the lower right plot of Fig. 12, shows that the bounds can be drastically tightened if the correlation between the three AQGC is resolved. Differential distributions will certainly provide this information, so that a $\gamma\gamma$ collider should be able to constrain AQGC by an order of magnitude better than an e^+e^- collider operating at comparable energy.

7 Summary

A Monte Carlo generator, which is based on multi-channel techniques with adaptive self-optimization, has been constructed for lowest-order predictions for the processes $\gamma\gamma \to 4f$ and $\gamma\gamma \to 4f\gamma$. Fermions are treated in the massless approximation. Anomalous triple and quartic gauge-boson couplings, as well as an effective $\gamma\gamma H$ coupling, are included in the transition matrix elements for $\gamma\gamma \to 4f$. For $\gamma\gamma \to 4f$ compact results for the helicity amplitudes are presented in terms of Weyl–van der Waerden spinor products.

Using this generator, we have presented a variety of numerical results.

(1) A representative list of integrated cross sections for the processes $\gamma\gamma \to 4f$ and $\gamma\gamma \to 4f\gamma$ is compared to results obtained with the Whizard/Madgraph package. We find agreement between both Monte Carlo programs.

(2) The dependence of some $\gamma\gamma \to 4f$ and $\gamma\gamma \to 4f\gamma$ cross sections on the CM energy is shown. In this context, the influence of a realistic photon beam spectrum and the size of subcontributions originating from charged-current, neutral-current, or strong interactions are investigated.

(3) The complete lowest-order cross section for $\gamma\gamma \to WW \to 4f$ is compared with the corresponding double-pole approximation, revealing an accuracy of the latter of 1−3%. While this deviation is of the naively expected order of Γ_W/M_W, the gauge-variant subset of diagrams with two resonant W bosons, the so-called "CC03" signal diagrams, yields differences of 5−10% to the full calculation. The deviations of the naive signal grow with increasing energy, whereas the quality of the double-pole approximation remains stable.

(4) Different schemes for introducing a finite width for gauge bosons are analyzed, and good agreement between the gauge-invariant complex-mass scheme and the fixed-width scheme is found. However, the results also reveal problems (at least in $\gamma\gamma \to 4f\gamma$) when using the running width.

(5) A few differential distributions are discussed for $\gamma\gamma \to 4f$ processes that proceed via charged-current interactions, in particular comprising distributions in the invariant mass and in the production angle of reconstructed W bosons and in the invariant mass of a resonant Higgs boson. Moreover, it is shown that the convolution over the photon spectrum significantly distorts energy and angular distributions of the produced fermions due to an effective photon polarization.

(6) Finally, we examine the effects of anomalous triple and quartic gauge-boson couplings on $\gamma\gamma \to 4f$ cross sections. Since contributions of anomalous couplings to cross sections can cancel in specific configurations, it is necessary to take into account results from other observables (such as differential distributions) or from other experiments (such as e^+e^- or $e^-\gamma$ collisions) in order to constrain individual anomalous couplings. Our results suggest that an analysis of the processes $\gamma\gamma \to 4f$ can constrain anomalous $\gamma\gamma WW$ couplings about an order of magnitude better than studying $e^+e^- \to 4f\gamma$.

Apart from studying the processes $\gamma\gamma \to 4f$ and $\gamma\gamma \to 4f\gamma$ in lowest order the described event generator is a first step towards a precision calculation of the process $\gamma\gamma \to WW \to 4f$ which has to include radiative corrections to the dominating W-pair production process. In particular,

the results for the radiative processes $\gamma\gamma \to 4f\gamma$ can serve as a basic building block in this task. In a next step, we will complete the calculation of electroweak corrections in the double-pole approximation similar to the approach of RacoonWW for e^+e^- annihilation.

Acknowledgements. A. Denner is gratefully acknowledged for valuable discussions and for carefully reading the manuscript.

References

1. I.F. Ginzburg et al., Nucl. Instrum. Meth. **205**, 47 (1983); Nucl. Instrum. Meth. A **219**, 5 (1984); V.I. Telnov, Nucl. Instrum. Meth. A **294**, 72 (1990); R. Brinkmann et al., Nucl. Instrum. Meth. A **406**, 13 (1998) [hep-ex/9707017]; I. Watanabe et al., $\gamma\gamma$ collider as an option of JLC, KEK-REPORT-97-17; B. Badelek et al. TESLA Technical Design Report, Part VI, Chap. 1: Photon collider at TESLA, hep-ex/0108012; T. Abe et al. [American Linear Collider Working Group Collaboration], in Proceedings of the APS/DPF/DPB Summer Study on the Future of Particle Physics (Snowmass 2001), edited by R. Davidson, C. Quigg, SLAC-R-570, Resource book for Snowmass 2001 [hep-ex/0106055, hep-ex/0106056, hep-ex/0106057, hep-ex/0106058]
2. A. De Roeck, hep-ph/0311138; M. Krawczyk, hep-ph/0312341; S.J. Brodsky, hep-ph/0404186
3. G. Bélanger, F. Boudjema, Phys. Lett. B **288**, 210 (1992)
4. E.E. Boos, G.V. Jikia, Phys. Lett. B **275**, 164 (1992); D.A. Morris, T.N. Truong, D. Zappala, Phys. Lett. B **323**, 421 (1994) [hep-ph/9310244]; H.G.J. Veltman, Z. Phys. C **62**, 235 (1994) [hep-ph/9311261]; I.F. Ginzburg, I.P. Ivanov, Phys. Lett. B **408**, 325 (1997) [hep-ph/9704220]; E. Boos, V. Ilyin, D. Kovalenko, T. Ohl, A. Pukhov, M. Sachwitz, H.J. Schreiber, Phys. Lett. B **427**, 189 (1998) [hep-ph/9801359]; P. Niezurawski, A.F. Zarnecki, M. Krawczyk, JHEP **0211**, 034 (2002) [hep-ph/0207294]
5. I. Božović-Jelisavčić, K. Mönig, J. Šekarić, hep-ph/0210308
6. M. Moretti, Nucl. Phys. B **484**, 3 (1997) [hep-ph/9604303]; hep-ph/9606225; E. Boos, T. Ohl, Phys. Lett. B **407**, 161 (1997) [hep-ph/9705374]
7. M. Baillargeon, G. Bélanger, F. Boudjema, Phys. Lett. B **404**, 124 (1997) [hep-ph/9701368]
8. M. Baillargeon, G. Bélanger, F. Boudjema, Nucl. Phys. B **500**, 224 (1997) [hep-ph/9701372]
9. G. Tupper, M.A. Samuel, Phys. Rev. D **23**, 1933 (1981); S.Y. Choi, F. Schrempp, Phys. Lett. B **272**, 149 (1991); E. Yehudai, Phys. Rev. D **44**, 3434 (1991)
10. I.B. Marfin, V.A. Mossolov, T.V. Shishkina, hep-ph/0304250
11. G. Bélanger, G. Couture, Phys. Rev. D **49**, 5720 (1994); S.Y. Choi, K. Hagiwara, M.S. Baek, Phys. Rev. D **54**, 6703 (1996) [hep-ph/9605334]
12. M. Herrero, E. Ruiz-Morales, Phys. Lett. B **296**, 397 (1992) [hep-ph/9208220]; P. Poulose, L.M. Sehgal, Phys. Lett. B **552**, 57 (2003) [hep-ph/0211179]
13. A. Aeppli, G.J. van Oldenborgh, D. Wyler, Nucl. Phys. B **428**, 126 (1994) [hep-ph/9312212]
14. S. Jadach et al., Phys. Rev. D **61**, 113010 (2000) [hep-ph/9907436]; **65**, 093010 (2002) [hep-ph/0007012]; Comput. Phys. Commun. **140**, 432 (2001) [hep-ph/0103163]; **140**, 475 (2001) [hep-ph/0104049]
15. W. Beenakker, F.A. Berends, A.P. Chapovsky, Nucl. Phys. B **548**, 3 (1999) [hep-ph/9811481]
16. A. Denner, S. Dittmaier, M. Roth, D. Wackeroth, Nucl. Phys. B **560**, 33 (1999) [hep-ph/9904472]
17. A. Denner, S. Dittmaier, M. Roth, D. Wackeroth, Phys. Lett. B **475**, 127 (2000) [hep-ph/9912261]; LC-TH-2000-014 [hep-ph/9912447]; Nucl. Phys. B **587**, 67 (2000) [hep-ph/0006307]; hep-ph/0101257; Comput. Phys. Commun. **153**, 462 (2003) [hep-ph/0209330]
18. Y. Kurihara, M. Kuroda, D. Schildknecht, Phys. Lett. B **509**, 87 (2001) [hep-ph/0104201]
19. A. Denner, S. Dittmaier, R. Schuster, Phys. Rev. D **51**, 4738 (1995) [hep-ph/9411268]
20. A. Denner, S. Dittmaier, R. Schuster, Nucl. Phys. B **452**, 80 (1995) [hep-ph/9503442]
21. G. Jikia, Nucl. Phys. B **494**, 19 (1997) [hep-ph/9612380]
22. I.B. Marfin, V.A. Mossolov, T.V. Shishkina, hep-ph/0305153; hep-ph/0401068
23. D.Y. Bardin, S. Riemann, T. Riemann, Z. Phys. C **32**, 121 (1986); F. Jegerlehner, Z. Phys. C **32**, 425 (1986) [Erratum C **38**, 519 (1988)]; A. Denner, T. Sack, Z. Phys. C **46**, 653 (1990)
24. K. Melnikov, O.I. Yakovlev, Nucl. Phys. B **471**, 90 (1996) [hep-ph/9501358]; W. Beenakker, A.P. Chapovsky, F.A. Berends, Phys. Lett. B **411**, 203 (1997) [hep-ph/9706339]; Nucl. Phys. B **508**, 17 (1997) [hep-ph/9707326]; A. Denner, S. Dittmaier, M. Roth, Nucl. Phys. B **519**, 39 (1998) [hep-ph/9710521]
25. F.A. Berends, R. Pittau, R. Kleiss, Nucl. Phys. B **424**, 308 (1994) [hep-ph/9404313]; Comput. Phys. Commun. **85**, 437 (1995) [hep-ph/9409326]; F.A. Berends, P.H. Daverveldt, R. Kleiss, Nucl. Phys. B **253**, 441 (1985); J. Hilgart, R. Kleiss, F. Le Diberder, Comput. Phys. Commun. **75**, 191 (1993)
26. R. Kleiss, R. Pittau, Comput. Phys. Commun. **83**, 141 (1994) [hep-ph/9405257]
27. A.F. Zarnecki, Acta Phys. Polon. B **34**, 2741 (2003) [hep-ex/0207021]
28. V. Telnov, Nucl. Instrum. Meth. A **355**, 3 (1995); P. Chen, T. Ohgaki, A. Spitkovsky, T. Takahashi, K. Yokoya, Nucl. Instrum. Meth. A **397**, 458 (1997) [physics/9704012]
29. K.J.F. Gaemers, G.J. Gounaris, Z. Phys. C **1**, 259 (1979); K. Hagiwara, R.D. Peccei, D. Zeppenfeld, K. Hikasa, Nucl. Phys. B **282**, 253 (1987); M.S. Bilenky, J.L. Kneur, F.M. Renard, D. Schildknecht, Nucl. Phys. B **409**, 22 (1993)
30. G. Gounaris et al., in Physics at LEP2, edited by G. Altarelli, T. Sjöstrand, F. Zwirner, CERN 96-01, Vol. 1, p. 525, hep-ph/9601233
31. G. Bélanger, F. Boudjema, Phys. Lett. B **288**, 201 (1992); O.J. Eboli, M.C. Gonzalez-Garcia, S.F. Novaes, Nucl. Phys. B **411**, 381 (1994) [hep-ph/9306306]; G. Abu Leil, W.J. Stirling, J. Phys. G **21**, 517 (1995) [hep-ph/9406317]; W.J. Stirling, A. Werthenbach, Eur. Phys. J. C **12**, 441 (2000) [hep-ph/9905341]; **14**, 103 (2000) [hep-ph/9903315]
32. A. Denner, S. Dittmaier, M. Roth, D. Wackeroth, Eur. Phys. J. C **20**, 201 (2001) [hep-ph/0104057]
33. W. Kilian, WHIZARD 1.0: A generic Monte-Carlo integration and event generation package for multi-particle processes. Manual, LC-TOOL-2001-039

34. T. Stelzer, W.F. Long, Comput. Phys. Commun. **81**, 357 (1994) [hep-ph/9401258]; H. Murayama, I. Watanabe, K. Hagiwara, HELAS: HELicity amplitude subroutines for Feynman diagram evaluations, KEK-91-11
35. M.W. Grünewald et al., in Reports of the Working Groups on Precision Calculations for LEP2 Physics, edited by S. Jadach, G. Passarino, R. Pittau (CERN 2000-009, Geneva, 2000), p. 1 [hep-ph/0005309]
36. M. Böhm, H. Spiesberger, W. Hollik, Fortsch. Phys. **34**, 687 (1986); A. Denner, Fortsch. Phys. **41**, 307 (1993); A. Denner, S. Dittmaier, G. Weiglein, Nucl. Phys. B **440**, 95 (1995) [hep-ph/9410338]
37. K. Fujikawa, Phys. Rev. D **7**, 393 (1973); M. Bace, N.D. Hari Dass, Annals Phys. **94**, 349 (1975); B.W. Lee, R.E. Shrock, Phys. Rev. D **16**, 1444 (1977); M.B. Gavela, G. Girardi, C. Malleville, P. Sorba, Nucl. Phys. B **193**, 257 (1981); N.G. Deshpande, M. Nazerimonfared, Nucl. Phys. B **213**, 390 (1983); F. Boudjema, Phys. Lett. B **187**, 362 (1987)
38. D. Bardin et al, in Physics at LEP2, edited by G. Altarelli, T. Sjöstrand, F. Zwirner, CERN 96-01, Vol. 2, p. 3, hep-ph/9709270
39. S. Dittmaier, Phys. Rev. D **59**, 016007 (1999) [hep-ph/9805445]
40. E.N. Argyres et al., Phys. Lett. B **358**, 339 (1995) [hep-ph/9507216]; W. Beenakker et al., Nucl. Phys. B **500**, 255 (1997) [hep-ph/9612260]
41. S. Dittmaier, M. Roth, Nucl. Phys. B **642**, 307 (2002) [hep-ph/0206070]
42. W. Beenakker et al., in Physics at LEP2, edited by G. Altarelli, T. Sjöstrand, F. Zwirner (CERN 96-01, Geneva, 1996), Vol. 1, p. 79 [hep-ph/9602351]
43. G.J. Gounaris, J. Layssac, F.M. Renard, Phys. Rev. D **61**, 073013 (2000) [hep-ph/9910395]; **62**, 073012 (2000) [hep-ph/0005269]
44. G. Bélanger, F. Boudjema, Y. Kurihara, D. Perret-Gallix, A. Semenov, Eur. Phys. J. C **13**, 283 (2000) [hep-ph/9908254]
45. M.A. Shifman, A.I. Vainshtein, M.B. Voloshin, V.I. Zakharov, Sov. J. Nucl. Phys. **30**, 711 (1979) [Yad. Fiz. **30**, 1368 (1979)]
46. M. Roth, doctoral thesis, hep-ph/0008033
47. K. Hagiwara et al. [Particle Data Group Collaboration], Phys. Rev. D **66**, 010001 (2002)
48. A. Djouadi, J. Kalinowski, M. Spira, Comput. Phys. Commun. **108**, 56 (1998) [hep-ph/9704448]